

INFRASOUND ANALYSIS OF I18DK, NORTHWEST GREENLAND

MASTER THESIS

BY

CORNELIS WEEMSTRA

NOVEMBER 2008 - AUGUST 2009

Supervisors:

Dr. L.G. Evers

Royal Netherlands Meteorological Institute - Department of Seismology

Dr. J.A.M. Paulssen

Utrecht University - Division of Seismology

Contents

1	Introduction	7
1.1	General considerations to infrasound	7
	What is infrasound	7
	The medium	8
1.2	Why measure infrasound	10
1.3	Station siting	11
	Station environment	11
	Potential sources	11
	Atmosphere	15
1.4	Study objective	16
2	Analysis: Theory	19
2.1	The microbarometer	19
2.2	Array response pattern	21
2.3	Fisher analysis	27
	Time-domain data processing	27
	Frequency-domain data processing	31
3	Analysis: Results	33
3.1	Data, Filtering and Processing	33
	The data	33
	The filter	34
	Processing parameters	34
3.2	0.1 - 1.0 Hz band	36
	Basic processing results	36
	Back-azimuth variation	36
	Waveform	42
3.3	1.0 - 6.0 Hz band	44
	Basic processing results	44
	Back-azimuth variation	48
	Waveform	51

4 Interpretation & Discussion	53
4.1 Local weather dependence	53
Wind dependency	53
Temperature dependency	58
4.2 Microbaroms	60
Medium dependency	60
Source regions	60
4.3 1.0 - 6.0 Hz band sources	64
5 Conclusions	71

Abstract

Within the scope of the Comprehensive Nuclear-Test-Ban Treaty (CTBT), four methods are used to verify the treaty. One of these methods is based on the detection of infrasound waves generated by a nuclear explosion. Seismological, hydroacoustical and radionuclide measurements are also applied. The International Monitoring System (IMS) will consist of 60 infrasound stations of which 35 stations are currently operational. The goal of this MSc Research is to process and subsequently interpret the data obtained from an infrasound station situated on the northwestern shoreline of Greenland. This station is operated by Denmark and labeled as I18DK. I18DK is situated in an area which receives an ever increasing attention from a geophysical perspective.

I18DK has continuously been operational from April 2003 and onwards. I18DK is an infrasound array with an aperture of about 1200 meters, where air-pressure fluctuations are recorded by eight microbarometers at a sample-rate of 20 Hz. The data are filtered in two bandwidths, which are both processed based on Fisher-statistics afterwards. The first bandwidth ranges from 0.1 up to 1.0 Hz, while a second analysis is performed on data between 1.0 and 6.0 Hz. Both bandwidths yields interesting results.

Several different source types are known to generate infrasound, for example, calving of icebergs and glaciers, explosions, earthquakes, oceanic wave-wave interaction, volcanic eruptions and aurora. The challenge is to distinguish between these different source types and use the outcome of the array analysis to better understand these phenomena. Microbaroms are by far the most frequent signals in the 0.1-1.0 Hz band. Their direction of origin can be related directly to oceanic wave-wave interaction intensity of *Kedar et al.* (2008). Furthermore, can their detectability be related to the wind direction at upper stratospheric levels.

The rate of occurrence of icequakes and the calving of glaciers is of interest in relation to global warming. The glaciers south of I18DK produce significant infrasound during summer time. A direct link can be found between the number of warm days in a year and the number of infrasound detections from a north-northeast direction. These signals seem to be generated by run-off of water from the local ice cap north of I18DK.

Chapter 1

Introduction

This introduction consists of four sections used to introduce infrasound and its propagation in general (1), answer the 'why' question concerning the general measurement of infrasound (2), introduce the station and describe the station siting and local atmospheric conditions (3) and finally to stress why specifically this station is of interest (4), i.e. the study objective.

1.1 General considerations to infrasound

What is infrasound

Infrasound is defined by sound waves with frequencies lower than 20 Hz. Due to its low frequency content, infrasound waves are able to travel over enormous distances. The lower frequencies are attenuated less as they propagate through the atmosphere. It can be compared to the basses of a stereo that penetrate deeper into the walls of your house. Just as infrared light is invisible to the human eye and acts at the lower end of the visible light spectrum, infrasound waves are inaudible to humans and they act at the lower end of the audible sound spectrum (20 - 20,000 Hz). In general the pressure fluctuations corresponding to infrasound are in the order of hundredths to tens of pascals with respect to a standard background pressure of approximate 1000 hPa. Acoustic waves travel with the speed of sound, i.e. 343 m/s at the earth's surface for a temperature of 20 °C.

When the wavelengths of infrasound waves become too long, gravity is becoming a factor influencing the linear relation between displacement and restoring force [*Gossard and Hooke* (1975)]. That is, from 0.01 Hz downwards the pressure waves are called acoustic-gravity waves and below 0.002 Hz the gravity becomes the restoring force. In this thesis only inaudible, non-gravity affected pressure waves are considered, i.e. infrasound. This means that frequencies lower than 0.01 Hz will not be taken into account and discussed.

In general, infrasound is generated when a large volume of air is displaced [*Evers* (2008)]. Phenomena able to do so are possible sources of infrasound. The following list gives a number of these sources [*Evers* (2008)]: airplanes (sub-sonic as well as super-sonic), aurora,

snow avalanches, chemical explosions, gas flares, lightning, meteors, nuclear tests, oceanic waves (generate the so-called microbaroms), severe weather and volcanoes. For a more thorough description of the characteristics of these sources, *Evers* (2008) can be consulted.

All of the above listed sources have the potential of being extremely powerful. For example, volcano eruptions have proven to be very powerful. These eruptions are able to produce low frequency sound waves with very high amplitudes as *Marchetti et al.* (2009) show. They assume a monopole source and correct the measured amplitudes for geometrical spreading. For the most powerful of the four examined volcanoes they find excess pressures up to 10^5 Pa at the source location. The first instrumentally recorded infrasound event ever was produced by the explosion of the Krakatoa west of Java, Indonesia on 1883, August 27. The infrasound was recorded on traditional barographs and traveled around the world seven times [*Symons* (1888)].

The medium

The speed of sound for an ideal gas is given by:

$$C_{ideal} = \sqrt{\gamma_g R_c T_a} \quad (1.1)$$

where γ_g gives the ratio of the specific heats, R_c is the gas constant and T_a represents the absolute temperature. This equation applies only when the sound wave is a small perturbation with respect to the ambient pressure. For air at room temperature, the multiplication of γ_g with R_c equals $402.8 m^2 s^{-2} K^{-1}$ and so the speed of sound in air is given by:

$$C_{air} = \sqrt{402.8 T_a} \quad (1.2)$$

The atmosphere influences infrasound propagation, with the composition, temperature and wind as the important controlling variables. Using equation 1.1 for C_{ideal} and taking into account this wind effect as well, *Gossard and Hooke* (1975) describe the so-called effective sound:

$$C_{eff} = \sqrt{\gamma_g R_c T_a} + \hat{n}_{xy} \cdot \bar{u} \quad (1.3)$$

The inner product between the wind speed vector \bar{u} and the unit vector \hat{n}_{xy} gives the contribution of the wind for infrasound waves traveling from source location \bar{x} to receiver location \bar{y} . This means that C_{eff} is positively affected by wind vectors having a component in the direction of propagation and negatively affected by winds with a component opposing the propagation direction of the infrasound waves.

Refraction of infrasound follows from Snell's law and the bending of infrasound waves towards the earth's surface depends on the combined effect of temperature and the wind. As the temperature and wind vector change when traveling upwards through the atmosphere, so does the effective sound speed. In Figure 1.1 the temperature as function of altitude is given based on the average kinetic energy of the atoms, from the U.S. Standard Atmosphere [*NOAA et al.* (1976)]. Refraction of upwards propagating infrasound is possible if the effective sound speed exceeds the C_{eff} at the source location.

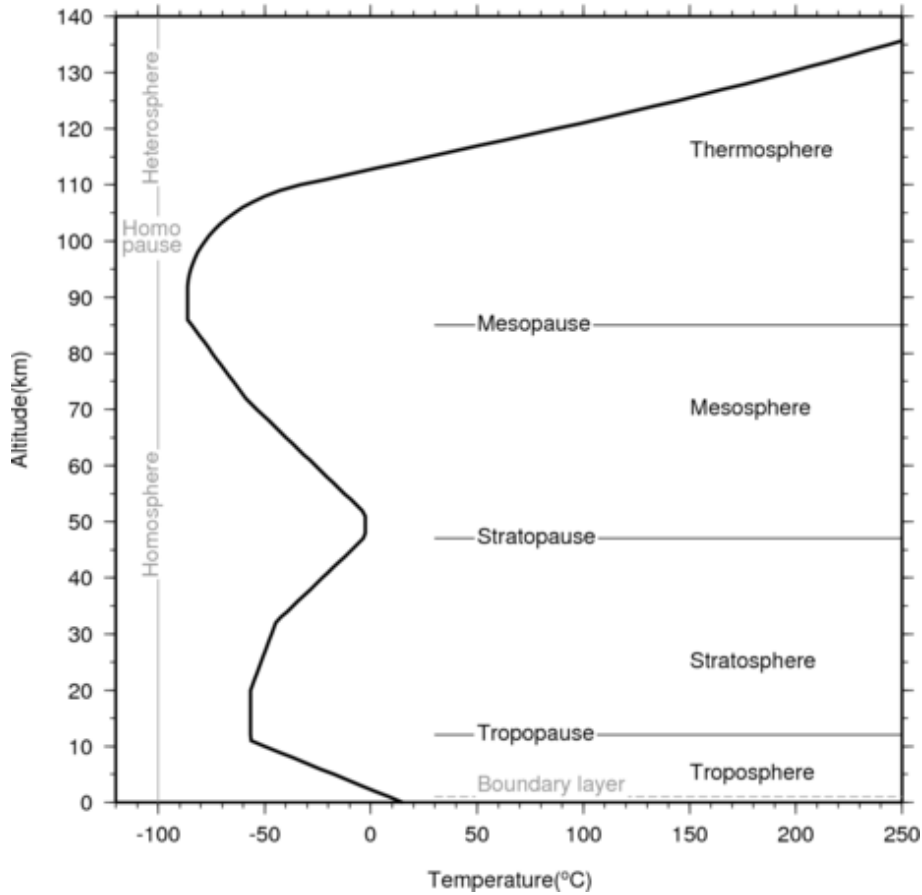


Figure 1.1: Temperature in the atmosphere as function of altitude from the U.S. Standard Atmosphere [NOAA *et al.* (1976)]. Values based on the average kinetic energy of the atoms. Figure adapted from *Evers* (2008).

As you can see in Figure 1.1 the atmosphere is divided into several layers. Naming of the layering in this figure is based on the sign the temperature gradient. For the study of infrasound this is most convenient [*Evers* (2008)]. From bottom to top the subsequent layers are named troposphere, stratosphere, mesosphere and thermosphere. Keep in mind however that Figure 1.1 is a standard atmosphere and variations with respect to this profile can be significant with geographical location and time.

C_{eff} relates to the square root of the temperature. The combined effect of this temperature effect and the contribution of the wind vector controls the refraction of infrasound waves. In general, due to the temperature increase with altitude in the stratosphere and thermosphere, these two layers have a high potential of acting as a duct for upward traveling infrasound waves [*Drob and Picone* (2003); *Evers and Schweitzer* (2010)].

Attenuation of infrasound is frequency dependent. *Bass et al.* (1972) show that both the classical amplitude absorption coefficient and the rotational amplitude absorption coefficient relate to the square of the frequency. As the total amplitude coefficient is the sum of these two coefficients, the attenuation of infrasound is related to the square of the

frequency.

1.2 Why measure infrasound

As elucidated already, because of its intrinsic characteristic low frequencies, infrasound can travel over enormous distances. This makes it a powerful instrument for a variety of purposes. The signature of the recorded signal is bipartitely dependent on the source and the medium. That is, infrasound signals can provide us with source characteristics as well as with information concerning the wind and temperature of the atmosphere. The challenge is to distinguish between these two contributions.

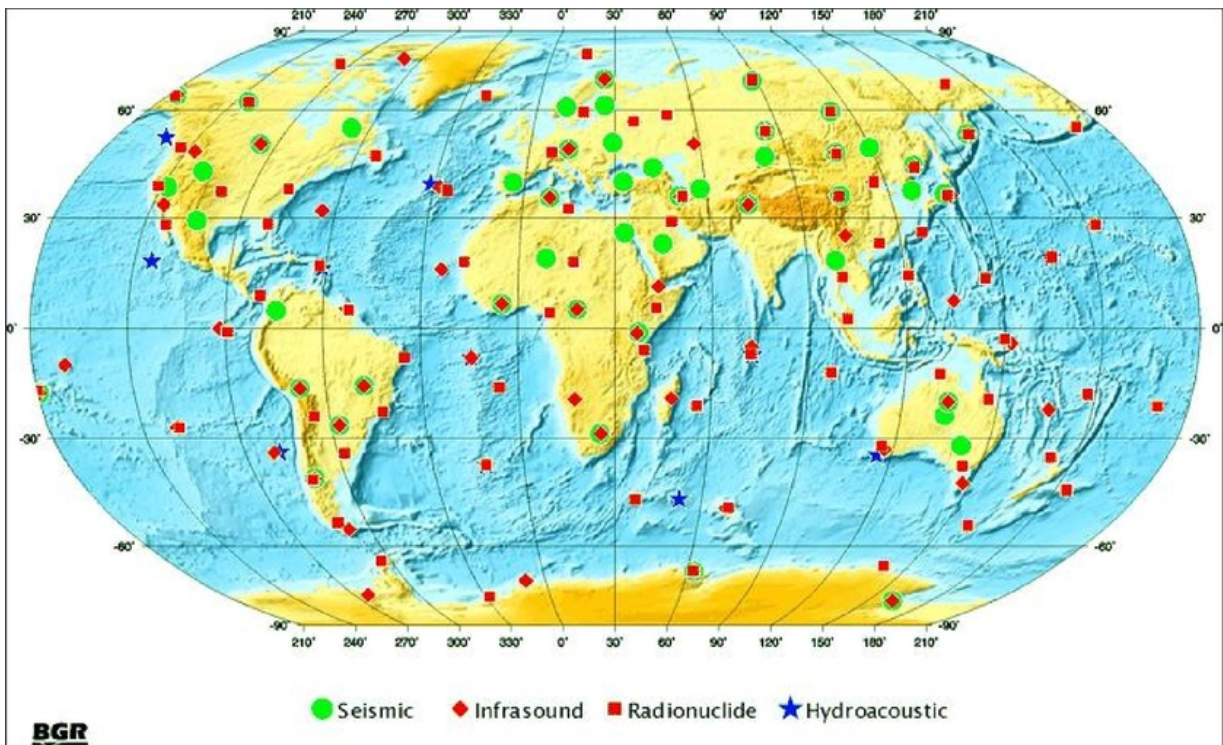


Figure 1.2: The International Monitoring System (IMS) of the CTBT. When the system will be in its final configuration, it shall comprise a total of 321 stations. 60 of these are meant for infrasound monitoring. The others will be hydroacoustic, radionuclide and seismological stations. The infrasound station I18DK is situated in the northwest of Greenland

The best known application of the analysis of infrasound is the verification of compliance of countries with the Comprehensive Nuclear-Test-Ban Treaty (CTBT). Within the scope of this treaty, four methods are used to verify compliance of the signatory states. One of these methods is thus based on the detection of infrasound waves generated by a nuclear explosion. Seismological, hydro-acoustical and radionuclide measurements are also applied to verify compliance. The International Monitoring System (IMS), being installed

by the Preparatory Commission for the Comprehensive Nuclear-Test-Ban Treaty Organization (CTBTO), will consist of 60 infrasound stations of which 35 stations are currently operational (Figure 1.2).

Evers (2008) provides a complete list of other purposes to measure infrasound, which are the following. Distinguish between earth's surface vibrations caused by solid earth sources and those originated by atmospheric sources. Provide information on the state of the atmosphere. Deduce from the recorded infrasound signal specific source characteristics in case of forensic investigations. The possibility to act as an early warning system in case of the possible threat of volcanic eruptions (ash or even pyroclastic flows). Give insight in weather dependent sound propagation over large ranges. As military activities could potentially be detected over large ranges, as military intelligence.

1.3 Station siting

Station environment

IMS station I18DK is situated in northwest Greenland and the station operator is Denmark. Its exact location can be seen in Figure 1.3. The coordinates of the I18DK are 77.47487°N and 290.70892°E. The array of microbarometers is situated on the northern shoreline of a large bay (Inglefield Bredning). The bay penetrates more than 100 km into the vast landmass of Greenland and off I18DK the bay is approximately 30 km in width. To the north, Piulip Nunâ, a 20 by 30 km peninsula, obstructs the line of sight when standing at the station site. The mean annual temperature at the site is approximately minus 9 °C and the mean temperatures during the meteorological summer, i.e. June, July and August, vary around 5 °C. From the the beginning of November till the end of January it's totally dark while from halfway April till the end of August the sunlight is present permanently.

A detailed map of the area can be seen on page 14. This geographic map shows the location of I18DK near the town of Thule as a red spot. Throughout this thesis the names of objects (towns, glaciers, capes etc.) shall be used as denoted on this map. Approximately 1.5 km to the NNE of I18DK, the Qânâq Gletscher is situated. This glacier used to carry ice from the local ice cap of Piulip Nunâ seawards. More towards the northwest, the Bryant Gletscher and Fan Gletscher used to do the same as well as the few glaciers on the east side of the peninsula. However, according to the local station operator, there isn't a single active glacier anymore at Piulip Nunâ for many years. In the following subsection, the sources which are likely to be found in the recordings due to the local environment and station siting will be discussed. Afterwards the regional state of the atmosphere will be treated.

Potential sources

Infrasound in the 0.1 - 6.0 Hz band has been analyzed during this research. Six years of data of I18DK have been processed. The processing theory, methods and parameters will

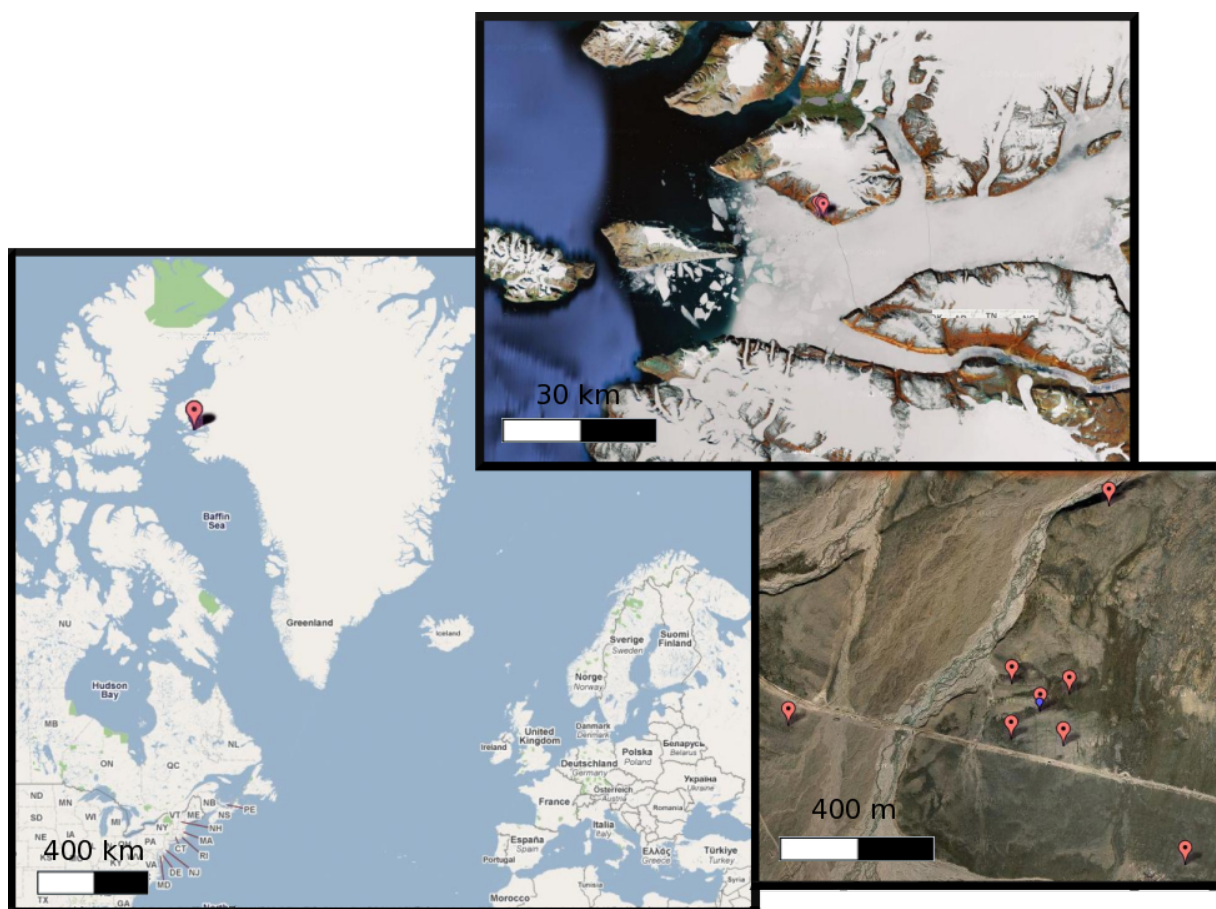


Figure 1.3: Map and satellite images showing the location and configuration of the I18DK infrasound array [Google Inc. (2009)]. The positions of the eight microbarometers on the south slope of the Piulip Nunâ peninsula are shown right down. At the top, the position of the station with respect to the bay and surroundings is shown. To put the satellite images in perspective: the width of the bay off the station is approximately 30 km for the top image and the distance between the two most right sensors in the right down image is about 1000 meters

be explained in later chapters, but it is important that the processing was performed twice: once after the data has been bandpass filtered in the frequency range 0.1 - 1.0 Hz and once for 1.0 - 6.0 Hz bandpass filtered data. For this reason the potential local sources as well as the regional infrasound sources of interest will be discussed here.

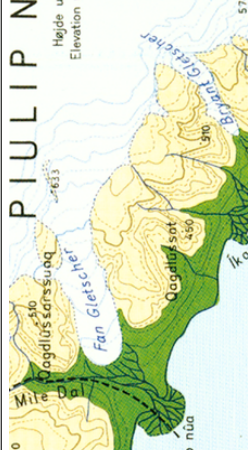
High frequency events are often associated to local sources due to the frequency dependent attenuation of infrasound. Therefore, the events in the 1.0 - 6.0 Hz bandpass filtered data, are more likely to be generated by local sources. Due to the remote location of I18DK, anthropogenic sources of infrasound ought not to be expected for these higher frequencies. The only possible anthropogenic infrasound could be generated in the town of Thule itself and to a less extend in one of the smaller settlements located at the other side of Inglefield Bredning (see page 14).

Considering the environment of I18DK, glaciers, avalanches, aurora, non-linear sea wave interaction (generating the so-called microbaroms) and severe weather are high potential sources for the recordings of I18DK. The United States National Oceanic and Atmospheric Administration showed in early performed research that snow avalanches are capable of generating acoustic signals in the frequency band of 1.0 – 5.0 Hz [Bedard Jr. *et al.* (1988); Bedard Jr. (1989); Bedard Jr. (1994)]. Wilson (1967) first discovered signals due the movement of large volumes of air in the upper atmosphere by aurora. The waveform generated by aurora depends on the type of aurora. Calving glacier ice and calving icebergs are capable of producing substantial infrasound signals [Campus (2004)]. The frequency of the signals generated by this calving glacier ice and these calving icebergs goes up to 4.0 Hz.

With the above probable sources in mind, it is important to have a good overview of the presence and distribution of active glaciers in the vicinity of I18DK. On the south side of Inglefield Bredning three glaciers are actively transporting ice towards the bay. From east to west these are called Misûmassoq, Politiken Broeand the Savage Gletscher. They are each between 500 meters and 1 km in width and the Misûmassoq and the Savage Gletscher are so-called tidal glaciers. These southern glaciers transport ice from the local ice cap south of Inglefield Bredning seawards. Towards the north, northeast and northwest, several large glaciers are continuously moving. These glaciers are a few orders of magnitude larger in size as the glaciers south of Inglefield Bredning and they range in width from 1.5 km to 7 km. Although not on the map of page 14, they are significant potential producers of infrasound. From east to west they are named the Heilprin Gletscher, the Tracy Gletscher, the Hubbard Gletscher, the Bowdoin Gletscher, the Tugto Gletscher, the Sun Gletscher, the Verhoeff Gletscher, the Morris Jesup Gletscher and the Diebitsch Gletscher respectively. They are all tidal glaciers.

In the band width of of 0.1 - 1.0 Hz, the microbaroms are an almost continuous background noise that peak around 0.2 Hz [Posmentier (1967)]. They were first described in 1939 by the seismologists Hugo Benioff and Beno Gutenberg at the California Institute of Technology, Pasadena. Their discovery was based on observations from an electromagnetic microbarograph. The theory describing the source mechanism of microbaroms was first developed by Posmentier (1967). He recognized that standing sea surface waves were able to radiate these microbaroms. His theory was further refined and rectified by Arendt and Fritts (2000), who provide the most recent thorough theoretical treatment concerning microbaroms generation.

Due to the fact that these standing surface waves can only be generated by opposite traveling sea surface waves having the same speed and frequency, only certain regions are capable of generating microbaroms. Intrinsic to the process generating the microbaroms is the fact that the frequency band in which the microbaroms are generated is relatively narrow. The same process is also responsible for the generation of microseisms, although the depth of the ocean is an important factor in microseism generation as well. That microbaroms and microseisms share a common source has been confirmed by Donn and Naini (1973) and Rind (1980), who correlated seismological and infrasound recordings from the same marine storm.



20 km



Kedar et al. (2008) generated ocean-wide wave-wave interaction intensity maps in the frequency range 0.07 - 0.15 Hz (i.e. microbaroms generation intensity maps in the frequency range 0.14 - 0.30 Hz [see e.g. *Posmentier* (1967)]) using Wave Action Models (WAM's). They show that two relatively large distinct regions on earth are susceptible to generate microbaroms. The first is southeast of Greenland, ranging from 50° - 65°N and 315° - 340°E approximately. The second is situated in the northern part of the Pacific and is centered around 40°N and 190°E having the approximate shape of a zonal elongated ellipse (Figure 4.8).

Atmosphere

The regional state of the atmosphere near I18DK shall be discussed in this subsection. This regional state of the atmosphere, with Thule as center of that region is of importance, because especially sound waves in the lower frequency range (0.1 - 1.0 Hz) can be refracted depending on these atmospheric conditions [see e.g. *Drob and Picone* (2003)].

The European Center for Medium range Weather Forecasting (ECMWF) makes use of ground-based weather station data and meteorological satellite data to produce atmospheric specifications and forecasts by means of rigorous statistics and geophysical fluid models. These ECMWF-forecasts are available 4 times daily up to a height of 60 km. Vertical resolution decreases from less than 25 meters at ground level to more than 5 km above 50 km altitude. In the region of northwest Greenland the geographical resolution of the models is 1.5°x 1.5°. Figure 1.4 shows the temporal variation of the atmospheric state variables temperature, zonal wind and meridional wind for 2004 at 76.5°N, 291.5°E. This is approximately 100 km south of I18DK. As the horizontal atmospheric gradients of these state variables are very small, this temporal profile is a good representation for the state of the atmosphere above I18DK.

Figure 1.4 shows the values of the state variables for every six hour interval over 2004 up to a height of approximately 60 km. Positive values mean westerly and southerly winds for the middle and top profile respectively. These profiles are roughly similar from year to year. The stratospheric zonal winds shift from eastwards to westwards at the end of spring and back at the end of the summer. This is the signature of the Arctic polar vortex, which coincides with the onset and end of the period with higher temperatures in the stratosphere.

Two polar vortices exist on earth. The Arctic polar vortex and the Antarctic polar vortex. In general, they are strongest during the hemisphere's winter and diminish or disappear during summer time. The polar vortices exist at mid and high-latitudes and in the upper troposphere and stratosphere. Dramatic temperature increases at upper stratospheric altitudes during spring cause the polar vortex at this altitude to weaken and reverse. Occasionally occurring Sudden Stratospheric Warmings (SSW's) during wintertime have the same effect. These SSW's only last for a few days.

In case of a hypothetical east-west symmetric source distribution with respect I18DK, the dominant back-azimuth for the lower frequency band would be west during winter time and east during summer time. The significantly higher temperature during summertime

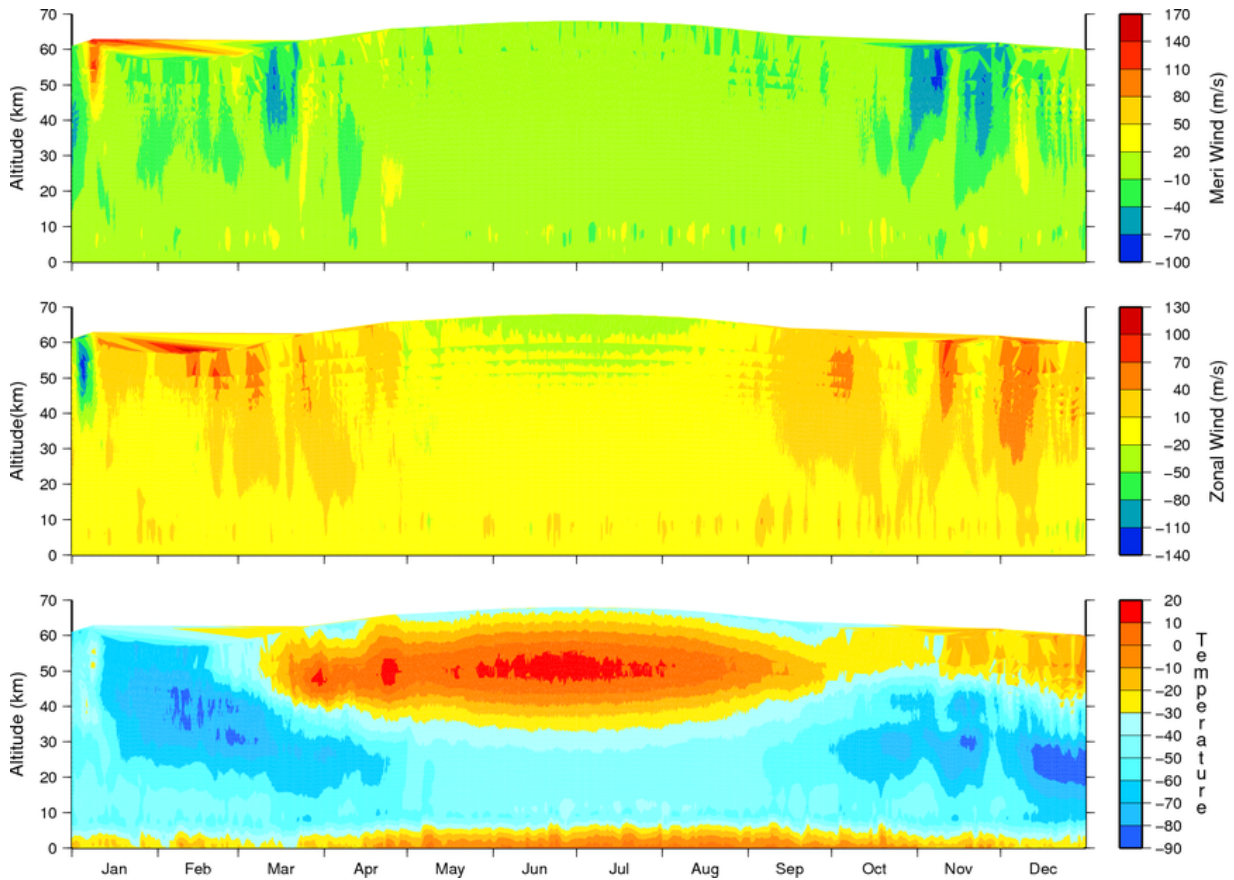


Figure 1.4: Three temporal profiles showing the state variables for every six hour interval over 2004 up to a height of approximately 60 km. From top to bottom the profiles represent the meridional wind, the zonal wind and the temperature respectively. Positive values represent southerly and westerly winds for the top and middle profile respectively. The state variables are extracted from ECMWF atmospheric analysis and the profiles shown are for 76.5°N , 291.5°E , which is approximately 100 km south of the location of I18DK.

in the upper stratosphere creates a better duct than during wintertime.

1.4 Study objective

With the signature of the Comprehensive Nuclear-Test-Ban-Treaty in 1996 the study of infrasound gained renewed interest. To apply infrasound measurements by I18DK successfully as verification of compliance with the CTBT, it is essential to gain insight into its characteristics. Distribution of sources, activity of these sources, temporal and directional variation of the medium characteristics and local station conditions all play together to make up the total station signature. One finally wishes to establish a station climatology with respect to its recording characteristics in order to unambiguously distinguish between sources. This temporal and directional variation of detectability of infrasound is station

specific due to the geographical variability of atmospheric conditions and source specifications. In the context of the CTBT verification, it would be desirable to build such a station climatology for each IMS station. Main objective of this thesis is to establish this for I18DK.

The I18DK-array continuously has been operational from April 2003 onwards. The data is filtered in two band widths, which are both processed based on Fisher-statistics afterwards. Secondary objective of this M.S. thesis is to link the frequency of occurrence and the direction of detected events to sources related to natural phenomena such as calving of ice from glaciers, snow avalanches and ocean wave interaction, i.e. microbaroms. The rate of occurrence of icequakes and the calving of glaciers is of interest in relation to global warming [see e.g. *Ekström et al. (2006)*].

Chapter 2

Analysis: Theory

2.1 The microbarometer



Figure 2.1: The DASE MB2000 microbarometer used by I18DK.

The microbarometers used for the measurement of infrasound at I18DK are French' DASE MB2000 microbarometers. These type of microbarometers are used for most of the IMS-stations and are absolute microbarometers. The actual recording is performed by a barometric capsule under vacuum made of Durinval alloy which is deflected by very small atmospheric pressure variations. The upper part of the casing of the MB2000 is filled with

the electronics, while the lower part makes up the measurement chamber, i.e. the volume connected to the open air (Figure 2.1). This measurement chamber is 0.6 liters containing the barometric capsule and is connected to ambient pressure by four 10 mm diameter inlets. The type of barometric capsule employed can measure pressure fluctuations around ambient pressure (1013 hPa at sea level). Measurements are taken in a frequency range extending from continuous (static pressure) to a few tens of Hertz. A high-resolution Linear Variable Differential Transformer (LVDT) is used to measure the micro deformation of the capsule (a few tens of nm/Pa).

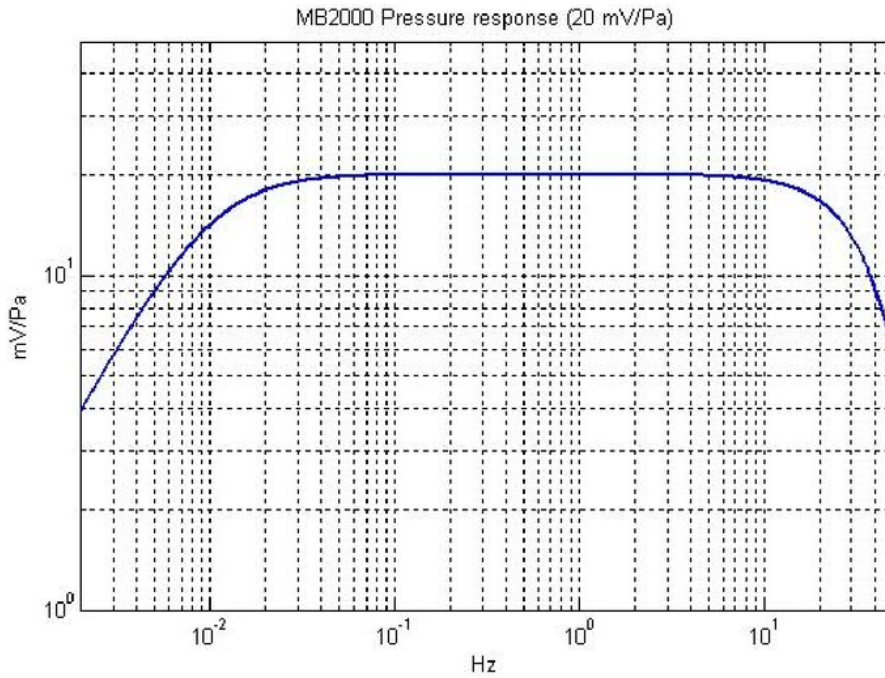


Figure 2.2: The frequency response of the DASE MB2000 microbarometer. The response is constant at 20 mV/Pa between 0.04 and 6.0 Hz.

The MB2000 can sense pressure variations under 1 mPa (instrumental noise being less than 2 mPa at 0.02 - 4 Hz). Using a sensitivity of 1 mV/Pa, the maximum pressure that can be sensed, is approximately 100 hPa. This gives the sensor a dynamic of 134 dB. However, the sensor's sensitivity is generally set to 20 mV/Pa to adapt it to the range of the digitizer, yielding a maximum sensible pressure level of 5 hPa and dynamic range 108 dB. This sensitivity increase involves removal of the DC component corresponding to atmospheric pressure. A high pass filter is applied, whose period can be adjusted from 800 s to 50 s. This means that the MB2000 microbarometer is principally highly differing from microbarometers based on differential acoustic pressures, like e.g. the KNMI microbarometer [Evers (2008)].

Figure 2.2 shows the pressure response with frequency. The infrasonic frequency range of interest is 0.002 to 20 Hz [Evers (2008)], but as the sample rate of the digitizers for I18DK is only 20 Hz, the presented pressure response has no use for pressure fluctuations

with a period less than 0.1 s, i.e. the Nyquist frequency. Furthermore the frequency response is only constant at a value of 20 mV/Pa for frequencies between 0.04 and 6.0 Hz.

2.2 Array response pattern

In general, a homogeneous random wavefield can be characterized by means of a spectral density function. Here, 'homogeneous random' means that the power of the frequencies of the wavefield do not change in space, although the frequency content is random. It is the same as a stationary wavefield. A frequency-wavenumber (f/k) spectral density function provides information about the frequency content of the wavefield as a function of the vector velocities and directions. For the assumption of a wavefield $g(t, \bar{r})$ at time t and location $\bar{r} = (x, y, z)$, the f/k density function is given by [see e.g. *Sherrif and Geldart (1995)*]

$$G(f, k_x, k_y, k_z) = \iiint \int_{-\infty}^{\infty} g(t, \bar{r}) e^{i(\bar{k} \cdot \bar{r} - 2\pi f t)} dt dx dy dz \quad (2.1)$$

where \bar{k} is the wavenumber vector which magnitude, $|\bar{k}|$, equals $2\pi/\lambda$, f the frequency and t the travel time.

This expression shows that if a certain frequency is highly present in a recording $g(t, \bar{r})$, the integration over the time domain will yield a high value for that specific frequency, as the product of the exponential term with $g(t, \bar{r})$ will yield a high value. In the same way, for frequencies less abundant in the recording, the integral of the product of the recording with the exponential term will be low, yielding a low spectral density for that frequency. For the k_x , k_y and k_z values, this principle works exactly the same.

We assume a monochromatic wavefield of unit amplitude in three dimensions described by

$$g(t, \bar{r}) = e^{i(2\pi f_0 t - \bar{k}_0 \cdot \bar{r})} \quad (2.2)$$

with frequency f_0 , and wavenumber $\bar{k}_0 = (k_{0x}, k_{0y}, k_{0z})$ at time t and location $\bar{r} = (x, y, z)$. This monochromatic wavefield can be written in the f/k domain using equation 2.1, leading to the following f/k spectral density function with the z -dependency still present:

$$G(f, k_x, k_y, z) = \delta(f - f_0) \delta(k_x - k_{0x}) \delta(k_y - k_{0y}) e^{-i k_{0z} z} \quad (2.3)$$

which for $z = 0$, i.e. the earth's surface and horizontal plane containing the microbarometers, becomes:

$$G(f, k_x, k_y) = \delta(f - f_0) \delta(k_x - k_{0x}) \delta(k_y - k_{0y}) \quad (2.4)$$

The maximum value for $G(f, \bar{k})$ is obtained at $f = f_0$ and $\bar{k} = \bar{k}_0$, while the f/k density function is zero for all other frequencies and wavenumbers.

Only Fourier transforming equation 2.2 in the time domain by

$$G(f, \bar{r}) = \int_{-\infty}^{\infty} g(t, \bar{r}) e^{-i 2\pi f t} dt \quad (2.5)$$

yields:

$$G(f, \bar{r}) = \delta(f - f_0) e^{-i\bar{k}_0 \cdot \bar{r}} \quad (2.6)$$

Now we return to the common situation of a non-monochromatic wavefield. The time Fourier transform (equation 2.5) of such a wavefield can be written in terms of the angular frequency ω instead of the oscillation frequency f , where $\omega = 2\pi f$. The time Fourier transform of the recording of the j^{th} station of a seismic array can be by

$$G(\omega, \bar{r}_j) = A_j(\omega) e^{i\varphi_j(\omega)} \quad (2.7)$$

where the amplitude $A_j(\omega)$ and phase information $\varphi_j(\omega)$ are specific for station j .

The Fourier transform of the cross-correlation, often simply called the cross-spectrum, is equivalent to the multiplication of the complex conjugate of the Fourier transform of the signal of the first station with the Fourier transform of the signal of the second station (cross-correlation theorem). Using the notation of equation 2.7, the cross-spectrum S_{jm} between the j^{th} and m^{th} station can be written as:

$$S_{jm}(\omega) = A_j(\omega) e^{-i\varphi_j(\omega)} \cdot A_m(\omega) e^{i\varphi_m(\omega)} \quad (2.8)$$

The modulus of S_{jm} in equation 2.8 will become high valued for those frequencies that are highly present in the signals. This is simply the product of the amplitude values $A_j(\omega)$ and $A_m(\omega)$. The phase of the cross-spectrum is given by the multiplication of the exponential terms.

Assuming the wavefield in the frequency-space domain and using the expression for the cross-spectrum, the power spectrum of the wavefield in the f/k domain in the discrete form is defined by *Smart and Flinn* (1971) as:

$$P(\omega, \bar{k}) = \sum_{j=1}^N \sum_{m=1}^N w(\bar{r}_j) w(\bar{r}_m) S_{jm}(\omega) e^{i\bar{k} \cdot (\bar{r}_j - \bar{r}_m)} \quad (2.9)$$

where spatial sampling is controlled by the number of sensors N located at positions $\bar{r}_j = (x_j, y_j, z_j)$. The weighting functions $w(\bar{r}_j)$ and $w(\bar{r}_m)$ describe the sensitivity of the stations j and m respectively and S_{jm} is the just described cross-spectrum between the j^{th} and m^{th} sensor. The phase of the exponential term in this expression depends on the inner product between \bar{k} and $(\bar{r}_j - \bar{r}_m)$ and corrects for the phase shift caused by the difference in station locations for the specific wavenumber vector \bar{k} . This difference in phase between the recordings of stations j and m is hidden in the cross-spectrum S_{jm} .

Equation 2.9 shows how for every station the cross-spectrum with each of the other stations is calculated. The value of the power spectrum depends on the correlation in the frequency domain between the signals of the two sensors j and m on the one hand and on the other hand on the placement of the two sensors with respect to each other $(\bar{r}_j - \bar{r}_m)$ by the exponential term.

Smart and Flinn (1971) showed that equation 2.9 can be rearranged to the product of two summations where one is the complex conjugate of the other one. Assuming all

sensors to be equally sensitive, the weights $w(\bar{r}_j)$ and $w(\bar{r}_m)$ can be regarded equal to unity. Subsequently rewriting equation 2.9 to

$$P(\omega, \bar{k}) = \sum_{j=1}^N A_j(\omega) e^{-i[\varphi_j(\omega) - \bar{k} \cdot \bar{r}_j]} \sum_{m=1}^N A_m(\omega) e^{i[\varphi_m(\omega) - \bar{k} \cdot \bar{r}_m]} \quad (2.10)$$

As the product of a variable with its complex conjugate is actually the modulus squared, this rearrangement reduces the amount of summations in the discretized f/k power spectrum to one, yielding a fast algorithm for computing frequency-wavenumber power spectra:

$$P(\omega, \bar{k}) = \left| \sum_{j=1}^N A_j(\omega) e^{i[\varphi_j(\omega) - \bar{k} \cdot \bar{r}_j]} \right|^2 \quad (2.11)$$

or substituting equation 2.7

$$P(\omega, \bar{k}) = \left| \sum_{j=1}^N G(\omega, \bar{r}_j) e^{-i\bar{k} \cdot \bar{r}_j} \right|^2 \quad (2.12)$$

For each wavenumber \bar{k} and angular frequency ω , a certain phase shift is expected with respect to a reference location $\bar{r}_0 = (0, 0, 0)$. Again, the exponential terms correct for the phase shifts of the stations \bar{r}_j with respect to the reference point $\bar{r} = (0, 0, 0)$. For a strong signal with a specific frequency traveling over the array with a specific velocity, the modulus of the summation in equation 2.12 will be high with respect to the value of the power spectrum for other frequencies and/or other velocities.

Using the time Fourier transform for the unit amplitude monochromatic three dimensional wavefield (equation 2.6) to find the estimate for $G(\omega, \bar{k})$ from equation 2.12 gives:

$$P(\omega, \bar{k}) = [\delta(\omega - \omega_0)]^2 \left| \sum_{j=1}^N e^{-i(\bar{k} - \bar{k}_0) \cdot \bar{r}_j} \right|^2 \quad (2.13)$$

From this equation, the array response is defined as:

$$R(\omega, \bar{p}) = \left| \frac{1}{N} \sum_{n=1}^N e^{-i\omega(\bar{p} - \bar{p}_0) \cdot \bar{r}_n} \right|^2 \quad (2.14)$$

where $R(\omega, \bar{p})$ is called the beam-forming array response pattern [Capon (1969)] and \bar{p} is the slowness vector which magnitude, $|\bar{p}|$, equals the inverse of the magnitude of the velocity vector.

The microbarometric fluctuations are measured in the horizontal plane of the earth's surface, i.e. \bar{r}_n 's only have horizontal components. For this reason, only the horizontal components of the slowness vectors are varied when a best beam search is performed. This reduces the equation for \bar{p}_0 to:

$$\bar{p}_0 = \frac{1}{\omega} (k_{0x}, k_{0y}) \quad (2.15)$$

Station	lon.(°)	lat.(°)	elev.(m)	x(m)	y(m)
I18L1	-69.2878	77.4756	87.5	0.0	0.0
I18L2	-69.2799	77.4807	140.0	194.0	565.0
I18L3	-69.2711	77.4717	30.0	407.0	-427.0
I18L4	-69.3167	77.4752	47.0	-699.0	-33.0
I18H1	-69.2910	77.4762	53.0	-80.0	85.0
I18H2	-69.2844	77.4760	71.0	80.0	48.0
I18H3	-69.2851	77.4747	46.0	62.0	-89.0
I18H4	-69.2911	77.4749	50.0	-82.0	-69.0

Table 2.1: Coordinates of the microbarometers of the I18DK-array as well as the relative coordinates used to produce the configuration in Figure 2.4 and the 2-dimensional array responses of Figure 2.5

The configuration of I18DK and the array responses for various frequencies are shown in Figure 2.4 and 2.5 respectively. The array responses are calculated, using the x/y values in table 2.1. This means that the differences in elevation of the eight microbarometers are not taken into account. As these vertical differences are relatively small with respect to the horizontal distances between the different sensors, this is a reasonable assumption. The x-and y-components of the slowness vector \bar{p} range from -0.005 s/m till 0.005 s/m.

The apparent sound speed c_{app} , i.e. the horizontal sound speed, and the back azimuth ϕ are related to the slowness vector in the following way:

$$\cos(\theta) |\bar{p}| = \frac{1}{c_{app}} \quad (2.16)$$

$$p_x = -\sin(\phi)(\cos(\theta) |\bar{p}|) \quad (2.17)$$

$$p_y = -\cos(\phi)(\cos(\theta) |\bar{p}|) \quad (2.18)$$

$$p_z = -\sin(\phi) |\bar{p}| \quad (2.19)$$

where θ is the inclination, i.e. the angle between the earth's surface and the slowness vector and z is positive from the earth's surface upwards. The earlier described effective sound speed C_{eff} takes into account wind and temperature effects and describes the propagation velocity of infrasound waves in the three dimensional domain and is related to c_{app} by $c_{app} = \frac{C_{eff}}{\cos\theta}$. Figure 2.3 shows a top view of the earth's surface with the projection of a wavefront propagating in a ENE direction. The back-azimuth equals 240° for this example.

Beam-forming is performed to resolve c_{app} and ϕ using the above equations. Considering the inclination of the incoming waves, the best beam is defined between two end-members. The former being signals which slowness vector \bar{p} only has a vertical component, so $\theta = 90^\circ$ and $C_{app} \rightarrow \infty$. This means that all sensors measure the waveform at the exact same moment in time. The latter end-member corresponds to an infrasound wave traveling parallel to the surface, which means that $c_{app} = C_{eff}$ and $\theta = 0$. For acoustic waves, this is the lowermost value of c_{app} that can be measured.

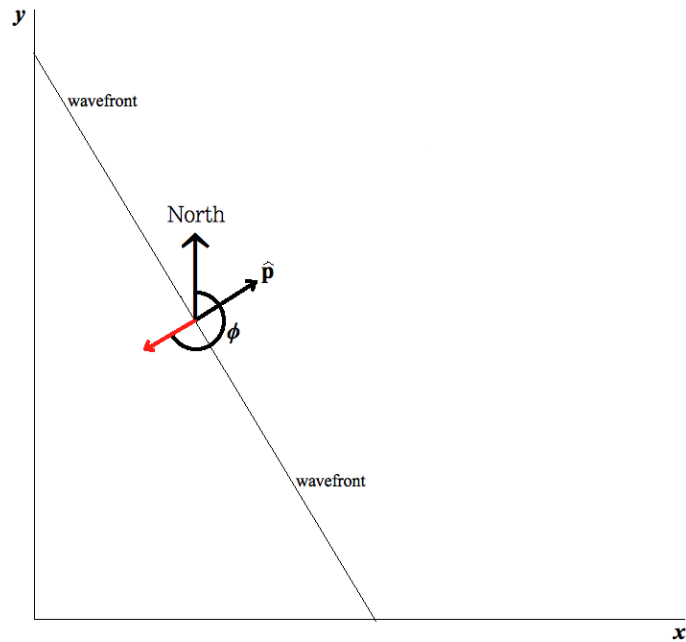


Figure 2.3: Top view on the earth's surface (xy -plane). The two dimensional slowness vector \bar{p} , aligned perpendicular to the wavefront, points into the direction of propagation along the surface. The angle between the North and the opposite of this propagation vector, indicated by the red arrow, is the back-azimuth ϕ .

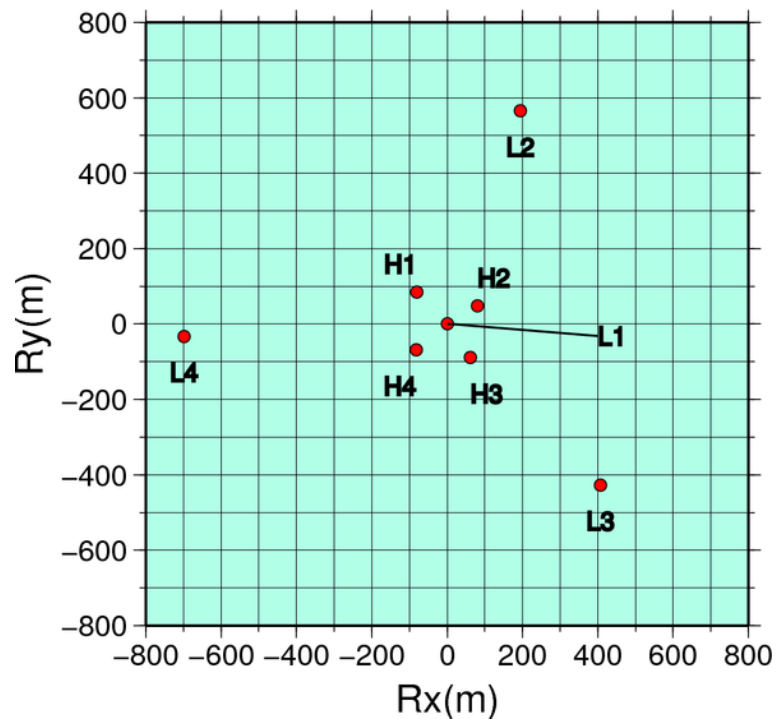


Figure 2.4: Array configuration of the I18DK-array. The corresponding array response is shown in Figure 2.5.

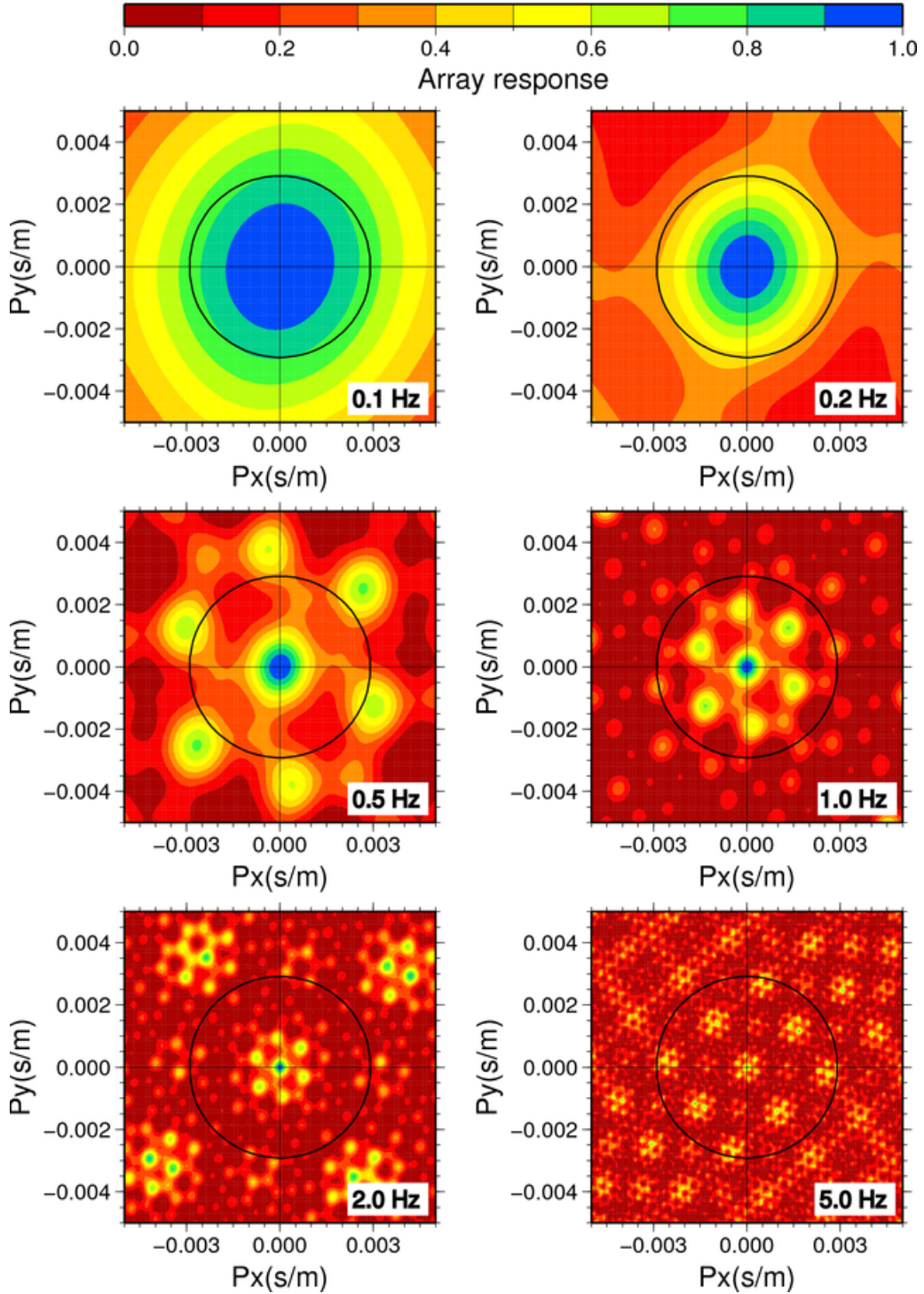


Figure 2.5: Array response of I18DK for six different frequencies in the case $\bar{p}_0 = 0$, i.e. a vertically incoming monochromatic wave. This vertical incident plane wave, i.e. $c_{app} = \infty$ and $\theta = 90^\circ$ peaks in the center for $p_x = p_y = 0$. The circle drawn in each of the six plots is for reference and corresponds to a horizontal velocity equal to the speed of sound at 20°C , i.e. 343 m/s.

Figure 2.5 shows that the main lobe has an approximate circular peak. As is required for an optimal array, most energy is present in the main lobe [Evers (2008)] and the side lobes' maximum values never exceed 0.8. There are six, roughly circular, side lobes surrounding the main lobe and their maximum values enter the slowness domain of interest above frequencies of 0.5 Hz. For a frequency of 0.1 Hz, the resolution in the slowness domain is low, which means that a broad range of directions and horizontal velocities are able to produce an array response close to the maximum. On the other hand, spatial aliasing starts to play a part at frequencies of 4.0 Hz approximately. As you can see in the plot representing the array response for a continuous signal of 5.0 Hz, there isn't a single solution. So several slowness vectors are able to produce the same maximum array response for that frequency.

2.3 Fisher analysis

Sophisticated processing of infrasound-array data is based on the analysis of variance by Fisher (1948). This general analysis of variance, in terms of a parent-set of N values (n_1, n_2, \dots, n_N) , makes use of randomly generating sub-sets of this parent-set. Deviations of individual values from the mean of the sub-set are independent of deviations of the mean of the sub-set from the mean of the parent-set. So the variances obtained for each sub-set are independent estimates of the overall variance. One probably can imagine that if these sub-set variances have values that lie close together, this means that there is no systematic pattern in the parent-set. However, this can only be concluded if for each of the sub-sets, all the possible constitutions of these sub-sets are evaluated. How this general theory of Fisher (1948) is applied to calculate the correlation between recordings is explained in the subsection below.

Time-domain data processing

After band pass filtering the data, the two frequency bands are analyzed individually. This analysis is performed for each time-window. Practically, the analysis involves a grid of $X \times X$ slowness vectors to be defined. This X is the number of different x- and y-components of the slowness vectors. The maximum slowness component defines the minimum omnidirectional horizontal velocity that is evaluated. Beam-forming for each of the X^2 slowness vectors is applied by time-shifting of the N recordings with respect to a reference station. These shifts in time basically mean shifts of a certain number of samples. The correlation between the traces is calculated for every slowness vector, yielding X^2 measures of correlation per time window. The highest correlation is, together with the corresponding horizontal velocity and back-azimuth, written to file. The measure of correlation used is the so-called Fisher ratio (F).

A total of $N = 8$ microbarometers is used in the analysis and the total number of samples per time window is $T = 256$, which means a 8×256 -Matrix is obtained. Beam-forming in the time domain is applied by time-shifting of the recordings, so the rows

containing the velocity values of the concerning component in the $N \times T$ -Matrix are shifted with respect to each other. In our case, the total number of slowness vectors ($X \times X$) evaluated is 10000, as $X = 100$. For each different slowness-vector \bar{p} , the Fisher ratio is calculated yielding a total of 10000 Fisher ratios. From these 10000 Fisher ratios, the highest corresponds to the best beam for the evaluated time window.

Returning to the Fisher ratio: the total data-set consists of recordings, an error-signal ϵ_{nt} due to uncorrelated noise and possible DC offsets. We assume that this uncorrelated noise ϵ_{nt} is normally distributed with a zero mean and variance σ^2 . Throughout this report, if we are talking about noise, we mean purely uncorrelated noise. The overall mean amplitude is given by

$$\bar{x} = \frac{1}{NT} \sum_{t=1}^T \sum_{n=1}^N x_{nt} \quad (2.20)$$

where x_{nt} are the individual samples of stations n at times t . This \bar{x} is used to remove the DC offset across the array due to variations on time scales exceeding the time window. The value of \bar{x} is the mean air pressure fluctuation of $8 \times 256 = 2048$ air pressure fluctuations.

After removing the DC offset, we are left with the data containing possible signals and uncorrelated noise. The deviation of each column from the overall average is $\alpha_t = \bar{x}_t - \bar{x}$, where \bar{x}_t is the mean amplitude across the array at time t :

$$\bar{x}_t = \frac{1}{N} \sum_{n=1}^N x_{nt} \quad (2.21)$$

This deviation α_t shows that the individual data values can be written as: $x_{nt} = \bar{x} + \alpha_t + \epsilon_{nt}$, or $x_{nt} - \bar{x} = \epsilon_{nt} + \alpha_t$. Stating the null hypothesis as the sample value of each individual sample in the $N \times T$ matrix being purely due to uncorrelated noise, means that the α_t values must be centered around zero for the null hypothesis to be valid.

In case of signal-coherence testing, the Fisher ratio is defined as the division of the “between sub-sample variance” by the “within sub-sample variance” [Melton and Bailey (1957)] where the “between sub-sample variance” is defined by:

$$V_t^2 = \frac{N}{T-1} \sum_{t=1}^T (\bar{x}_t - \bar{x})^2 \quad (2.22)$$

and the “within sub-sample variance” written as:

$$V_n^2 = \frac{1}{T(N-1)} \sum_{t=1}^T \sum_{n=1}^N (x_{nt} - \bar{x}_t)^2 \quad (2.23)$$

The descriptions “between sub-sample variance” and “within sub-sample variance” are based on how statisticians tend call the numerator and denominator of the Fisher ratio. A schematic representation of the ‘directions’ of the two variances is given in Figure 2.6.

Recalling the description of the general analysis of variance by Fisher in the first paragraph of this section: the sub-set equivalents are the columns of the $N \times T$ -Matrix, while

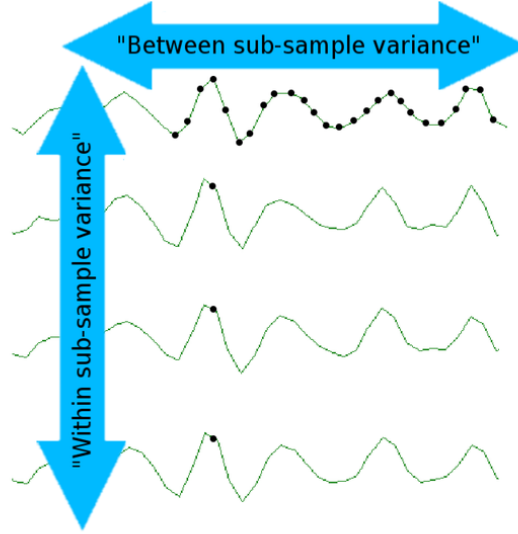


Figure 2.6: Schematic overview of the meaning of equations 2.23 and 2.22

the parent-set is represented by the whole matrix. The division of the two respective variances (equation 2.22 and 2.23) by each other gives the final expression for the Fisher ratio (F) [Melton and Bailey (1957)]:

$$F = \frac{V_t^2}{V_n^2} = \frac{T(N-1) \sum_{t=1}^T (\sum_{n=1}^N X_{nt})^2 - \frac{1}{T} (\sum_{t=1}^T \sum_{n=1}^N X_{nt})^2}{N(T-1) \sum_{t=1}^T \sum_{n=1}^N X_{nt}^2 - \frac{1}{N} \sum_{t=1}^T (\sum_{n=1}^N X_{nt})^2} \quad (2.24)$$

Melton and Bailey (1957) also derived a relation between the signal-to-noise power ratio (snr) on the traces, the signal-to-noise power ratio on the beam ($beam-snr$) and the Fisher ratio:

$$snr = \frac{1}{N} beam-snr = \frac{1}{N} (F - 1) \quad (2.25)$$

The lengthy Fisher ratio formula is difficult to comprehend, but the explanation of the division of the two variances (equations 2.22 and 2.23) by each other is intuitively easier to understand, because a low "within sub-sample variance" V_n^2 means that the signal values are highly alike yielding a high Fisher ratio. Likewise a high "between sub-sample variance" V_t^2 means that the sample values of the summed trace are highly differing in time, which is highly unlikely to be caused by the summation of independent noise, and thus points to a coherent signal, which indeed yields a high Fisher ratio and thus a low probability of the null-hypothesis (no coherent signal) explaining the data. So, highest Fisher ratios are obtained by high values of V_t^2 and low values of V_n^2 . Equation 2.24 can alternatively be interpreted as the division of the total energy of the summed signal minus the total energy of all samples by the sum of the energy of the individual samples minus the total energy of the summed signal. This is subsequently corrected by the number of degrees of freedom.

Considering the two variances again (equations 2.22 and 2.23), V_n^2 is a measure of the variance in signal as well as in noise and the result is a measure of noise power, while on

the other hand V_t^2 is measure of signal power only as it represents the variation common to all recordings with respect to the overall average \bar{x} . For the case of no signal present in the evaluated time window, i.e. $\alpha_t = 0$, the expected value for the "between sub-sample variance" and the "within sub-sample variance" are equivalent and given by:

$$E(V_t^2) = E(V_n^2) = \sigma^2 \quad (2.26)$$

where σ^2 is the variance of the assumed normally distributed uncorrelated noise again.

For the case of coherent energy traveling over the array, the "between sub-sample variance" will have an extra contribution represented by the non-zero α_t -term and the expected value of equation 2.22 is positively affected [*Evers* (2008)]:

$$E(V_t^2) = \sigma^2 + \frac{N}{T-1} \sum_{t=1}^T \alpha_t^2 \quad (2.27)$$

This subsequently gives a higher expected value for the Fisher ratio.

The expressions in equations 2.22 and 2.23 are in general characterized by two χ^2 distributions. We would like to obtain an unbiased estimate of the variance in both cases, given the number of degrees of freedom for the "between sub-sample variance", V_t^2 , to be $\nu_1 = (T - 1)$ and that corresponding to the "within sub-sample variance", V_n^2 , given by $\nu_2 = T(N - 1)$. The expected values for the Fisher ratio can be obtained by an F-test, which will yield a central F-distribution $F(\nu_1, \nu_2)$ if the null-hypothesis is true ,i.e. equation 2.26 is valid and only uncorrelated noise is recorded. A non-central F-distribution $F(\nu_1, \nu_2, \lambda_{nc})$ gives the distribution of the Fisher ratio in case coherent signal is present in the data. *Shumway* (1971) showed that the non-centrality parameter λ_{nc} is related to the degrees of freedom of the numerator and the signal-to-noise power ratio on the beam by $\lambda_{nc} = \nu_1 \times beam-snr$.

For longer time-windows, i.e. a higher T, the F-distributions become more peaked, more symmetrical and (more) separated. The average value for the central F-distribution, i.e. the expected Fisher ratio, becomes:

$$E(F) = \frac{\nu_2}{\nu_2 - 1} \simeq 1 \quad (2.28)$$

The non-central F-distribution is valid if there is some coherent energy recorded by the array ($\alpha_t \neq 0$) and the Fisher ratios are distributed according

$$E(F) = \frac{\nu_2(\nu_1 + \lambda_{nc})}{\nu_1(\nu_2 - 2)} \simeq beam-snr + 1 \quad (2.29)$$

In Figure 2.7 the Central F-distribution and non-central F-distribution for $\nu_1 = 255$ and $\nu_2 = 1792$ are shown. This corresponds to the number of time samples ($T = 256$) and stations ($N = 8$) used for the analysis. The non-central F-distribution is presented for $\lambda_{nc} = 127$, which corresponds to a *beam-snr* of 0.5. For a Fisher ratio of 1.25, the central Cumulative Distribution Function of F (central FCDF) has a value of 0.993 while

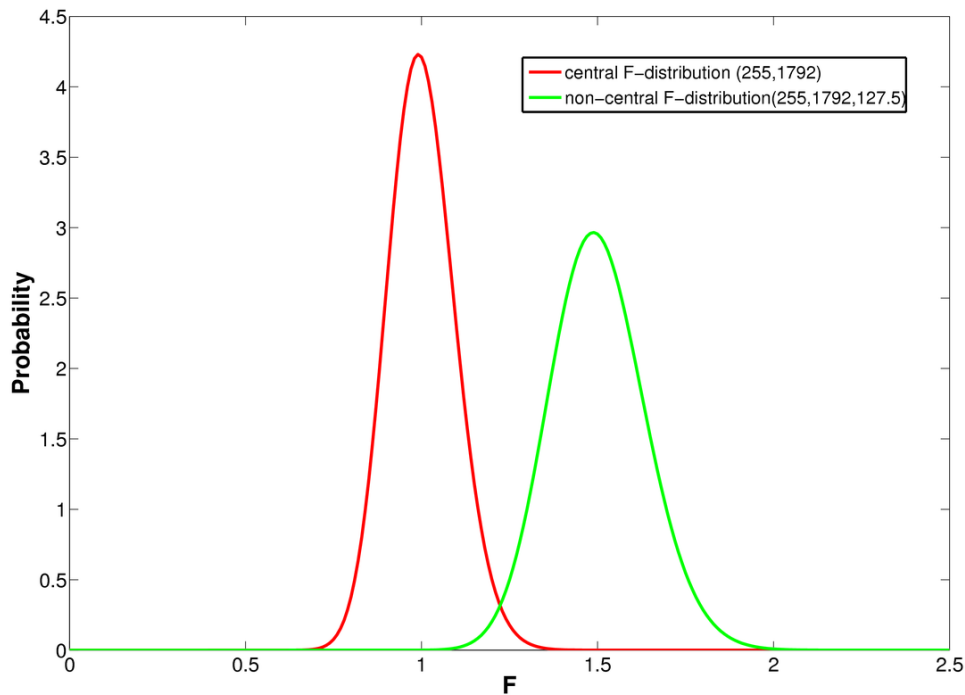


Figure 2.7: The central and non-central F-distributions for nominator degrees of freedom $\nu_1 = 255$ and denominator degrees of freedom $\nu_2 = 1792$. *beam-snr* corresponding to the non-centrality parameters of the non-central F-distribution is 0.5. This means that the mean *snr* on the traces is only 0.0625

the cumulative non-central F-distribution (non-central FCDF) has a value of 0.026. This practically means the following for this example: on the one hand, suppose a signal that exactly has a *beam-snr* of 0.5, i.e. a signal-to-noise power ratio on the traces (*snr*) of $0.5/8$, travels over the array. The chance that the array processing of the concerning time window will yield a $F < 1.25$, is 2.6%. Rejecting this Fisher ratio as being caused by uncorrelated noise is a type 2 error. On the other hand, if there is totally no coherent energy traveling over the array, the chance that the array processing will yield a $F > 1.25$ is 0.72%. Classifying this Fisher ratio as due to signal is a type 1 error.

Frequency-domain data processing

The equation applying Fisher statistics in the frequency-wavenumber domain was first derived by *Smart and Flinn* (1971). *Shumway* (1971) defined the Fisher ratio in this domain by the division of the signal power by the noise power, where the noise power in

the denominator is represented by the total energy minus the signal power:

$$F(\omega, \bar{k}) = \frac{P_S(\omega, \bar{k})}{P_T(\omega) - P_S(\omega, \bar{k})}(N - 1) \quad (2.30)$$

This explicitly shows that the Fisher ratio is a measure of the power of the signal to noise ratio.

For a signal traveling with a single frequency ω , the f/k power spectral density function for the array is given by equation 2.11:

$$P(\omega, \bar{k}) = \left| \sum_{j=1}^N G(\omega, \bar{r}_j) e^{-i\bar{k} \cdot \bar{r}_j} \right|^2 \quad (2.31)$$

where, $G(\omega, \bar{r}_n)$ are the Fourier transforms of the time shifted recordings of sensors n . In the presence of signal, equation 2.31 represents the signal power and it can be written as

$$P_S(\omega, \bar{k}) = \left| \frac{1}{N} \sum_{j=1}^N G(\omega, \bar{r}_j) e^{-i\bar{k} \cdot \bar{r}_j} \right|^2 = \frac{1}{N^2} P(\omega, \bar{k}) \quad (2.32)$$

The total amount of power in all the recordings is simply given by

$$P_T(\omega, \bar{k}) = \frac{1}{N} \sum_{j=1}^N |G(\omega, \bar{r}_j)|^2 \quad (2.33)$$

where the term related to the array response, $e^{-i\bar{k} \cdot \bar{r}_n}$, is not taken into account and so P_T incorporates the total amount of energy.

Chapter 3

Analysis: Results

This chapter first describes the processing sequence, the applied filter and the other processing parameters. Subsequent the results of the Fisher processing will be presented.

3.1 Data, Filtering and Processing

The data

In total, almost six years of data of I18DK are obtained. The data are retrieved on an external hard disk from the CTBTO's International Data Centre (IDC) in Vienna. Some gaps and the last three months of data are requested later on by means of the IDC's autoDRM interface. The data are obtained in the CSS 2.0 format. In order to deal with the raw data correctly, the program 'Geotool' (X Windows based graphics tool for displaying waveforms and performing basic analysis operations) is used to read the data and write it to ASCII files. Using the Seismic Analysis Code (SAC), maintained by the Incorporated Research Institutions for Seismology (IRIS), the ASCII files are converted to files in the SAC-format. This is done individually for each sensor, for every month.

During the above described procedure, it became clear that the raw data contain a considerable number of periods for which one or more of the sensors didn't produce a signal and/or the output trace was simply a zero amplitude trace. These periods range from less than 20 seconds to several days in some cases. Resulting processing variables are biased for such periods. For this reason the SAC month files are scanned for these periods and the begin-and end-times of these periods are stored in files. The processing results are corrected for these gaps later on, so for the time windows covered by such a period, the corresponding obtained variables are rejected from the result files. About 3 % of the data, i.e. the 3 % of the six years, are rejected this way.

The month files are cut up into day files, because this significantly increases the processing speed (less intermediate storage required). Fisher processing of the data is performed twice. Once after the data are band pass filtered between 1.0 and 6.0 Hz and once after they are filtered between 0.1 and 1.0 Hz. The results of the processing of the two pass

bands will be presented separately in two sections (3.2 and 3.3). Fisher processing is only performed in the time-domain.

Besides the 8 traces corresponding to the 8 microbarometers at I18DK, 4 additional channels are operational. These sensors measure the temperature, wind speed, wind direction and humidity level at the station site. These 4 channels have a sampling rate of 1 Hz. In the results and discussion sections these data are plotted simultaneously with the obtained processing variables from time to time.

The filter

Filtering of the data was put into effect using a Butterworth filter. The reason to use this filter is its frequency response, which is maximally flat in the passband and rolls off towards zero in the stopband (Figure 3.1). Furthermore, as distortion of signals is not desirable, forward and backward filtering was applied yielding a zero-phase shift of signal. The corner frequencies of a Butterworth filter are defined such, that the power at the corner frequency is half the power of the passband, since the power is the amplitude squared, the amplitude values at the corner frequencies are $\sqrt{\frac{1}{2}}$ of the filter amplitude in the passband. As well the 0.1 - 1.0 as the 1.0 - 6.0 Hz data are obtained after filtering the data with a 2nd order butterworth filter. This means that the power and amplitude at the corner frequencies are a factor 0.25 and 0.5 respectively with respect to their corresponding maximum passband values.

The formula describing the power ratio in decibels is given by:

$$L_{dB} = 10 \log_{10} \left(\frac{P_1}{P_0} \right) \quad (3.1)$$

where P_0 is the reference power with respect to which the difference in decibels of the prescribed power P_1 is evaluated. In the top plot of Figure 3.1 the decrease in dB with respect to this reference power (0dB) has been plotted against angular frequency for a corner frequency of $\frac{1.0}{2\pi}$. This plot shows the frequency response of a first order Butterworth filter.

Processing parameters

The sample rate of the 8 microbarometers of I18DK is 20 Hz. As is outlined already in section 2.3, the number of samples per analysis window is 256 (i.e. 12.8 s). The actual processing of the SAC-format day files is done after a few steps of cutting up few longer time windows into more shorter time windows. The files are cut up and written in the ASCII-format to files with a length of 10240 samples. This is 8 minutes and 32 seconds exactly. A single day spans 168 of these time windows. Because of the overlap of half a time window, 79 analysis windows of 12.8 s are processed. For each of these analysis windows, the highest Fisher ratio, corresponding back-azimuth and horizontal velocity are calculated. The attributes corresponding to the one analysis window of the 79 windows,

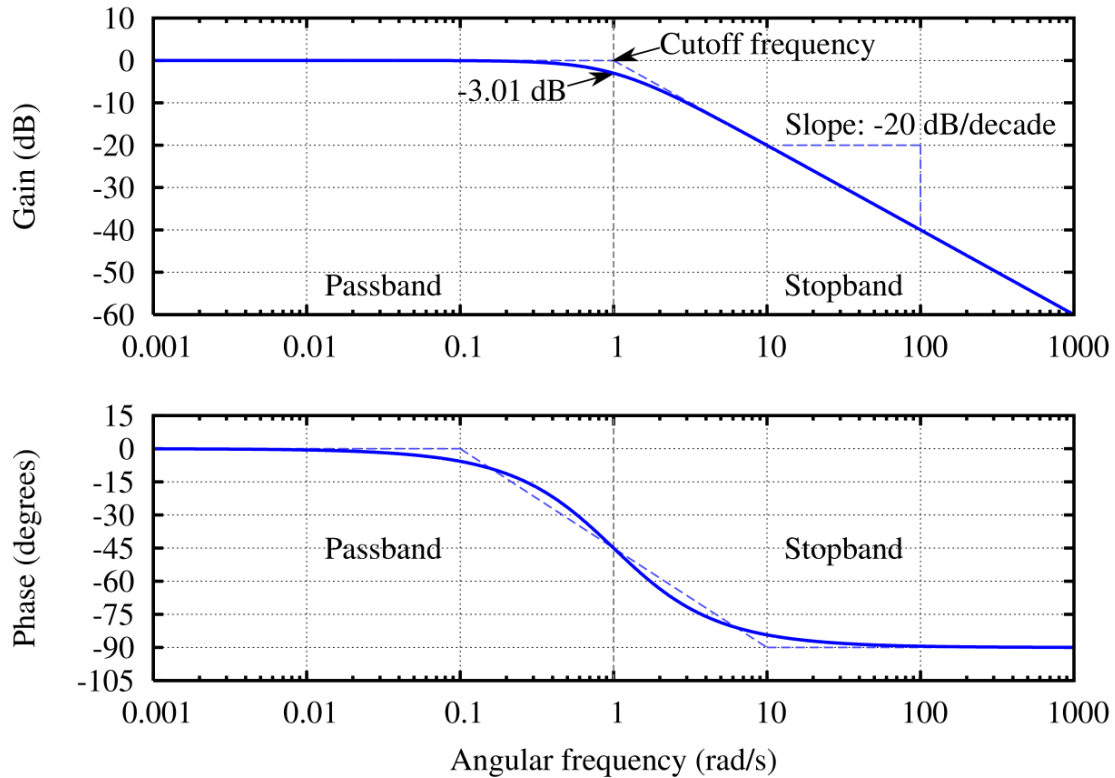


Figure 3.1: Frequency and phase response of a low pass Butterworth filter. The applied corner frequency is $\frac{1.0}{2\pi}$. The top plot shows the gain after only applying the filter once (1^{st} order filter). The decibel decrease of the power with respect to the reference power, which in this case is set to 0 dB, is plotted against angular frequency. The lower plot shows the phase shift after applying a forward Butterworth filter. This phase shift can be cancelled out by filtering the data backwards.

with the highest Fisher ratio are written to the result file. So 168 Fisher ratios and accompanying horizontal velocities and back-azimuths are calculated per day.

The choice for the lengths of the analysis windows and their degree of overlap is not arbitrary. The lengths of the analysis windows, i.e. 12.8 s, depends on the minimum velocity one wants to resolve and the aperture of the array. The maximum distance between two microbarometers of the I18DK-array is close to 1200 meters. The minimum velocity we would like to resolve is about 300 m/s, because this is approximately the lowest C_{eff} possible for the conditions at the station site, i.e. temperature and wind speed (see Figures 4.1 and 4.5 in this respect). This means that every signal will travel over the array in less than 4 seconds. So the analysis windows' lengths are long enough for the Fisher ratio to find any correlation if present. The length of the overlap between the subsequent time windows is 6.4 s and is needed to prevent short signals from being left undetected.

3.2 0.1 - 1.0 Hz band

Basic processing results

The processing results for this frequency band are presented in Figures 3.2, 3.3, 3.4 and 3.5. For each year the three calculated attributes are presented over time. For the sake of comparison, the same scales are used each year. In the top frames (a) the Fisher ratios are presented with the scale ranging from 0 to 500. A small number of the total number of Fisher ratios, exceeds this maximum scale value of 500. The wind speeds plotted in the same frame are the the daily mean wind speeds calculated from the measured wind speeds by I18DK. The middle frames (b) show the corresponding calculated apparent velocities with the vertical axis ranging from 150 m/s to 550 m/s. For the purpose of a clear distinction between the different values, the rejection of few of the horizontal velocity values exceeding the 550 m/s or ducking the minimum scale value of 150 m/s is accepted. This number is less than 5% however. The back-azimuth values are presented in the bottom frames (c).

Several remarkable features can be observed. First of all, during winter/early spring, the peaks in the Fisher ratios are higher and they occur more frequent. The Fisher ratios are relatively low in the period from the end of May till the end of November. There are still sharp peaks visible from time to time during this period, but these are less high. The lowest Fisher ratios in winter time are higher than the lowest Fisher ratios during summer time. For example, in the first three weeks of January of 2004, there seem to be no Fisher ratios having values lower than about 20. These observations seem to be yearly phenomena, although variable in strength (compare patterns for 2004 with 2005).

October and November appear to be the most windy months of the year. During the winter months (December, January, February and March) sharp peaks in the wind speed are visible for some years as well, but in general the mean wind speed is lower as during October and November. The peaks in the wind speed coincide with periods of low Fisher ratios and high scatter in horizontal velocity and back-azimuth. This anti correlation shall be addressed in section 4.1 of chapter 4.

The scatter in horizontal velocity and back-azimuth coincides with periods of relatively low Fisher ratios. During the earlier mentioned period, from the end of May till the end of November, the scatter is significantly higher, i.e. the best beams for the lower Fisher ratios show less consistent back-azimuth and horizontal velocity patterns. Most detections have horizontal velocities a bit lower than the speed of sound at the earth's surface for a temperature of 20 ° C, i.e. 343 m/s. That is, the center of the dark horizontal bands in the horizontal velocity plots seems to be around 335 m/s. The back-azimuth plots show two distinct bands. One around 120° and the other, less clear, around 280°.

Back-azimuth variation

In Figure 3.6 the temporal variation of the back-azimuth density with back-azimuth is presented. All events are taken into account, so no threshold Fisher ratio is applied to reject

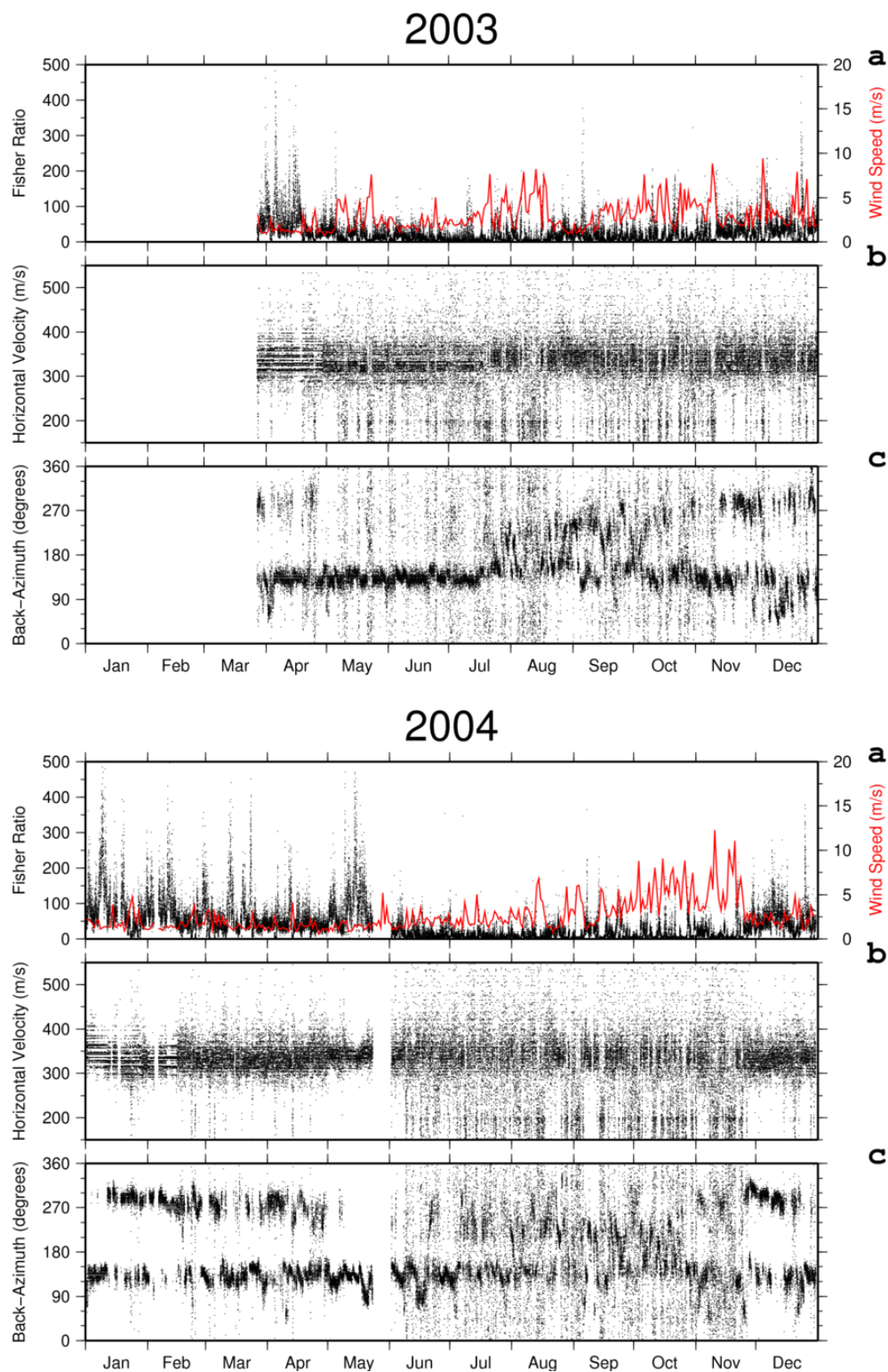


Figure 3.2: Processing results for 2003 & 2004. Frames **a** present the Fisher ratios. In the same frames, the wind speed is indicated by the red line. Frames **b** and **c** show the corresponding horizontal velocities and back-azimuths respectively. A gap in the infrasound data is present at the end of May, 2004.

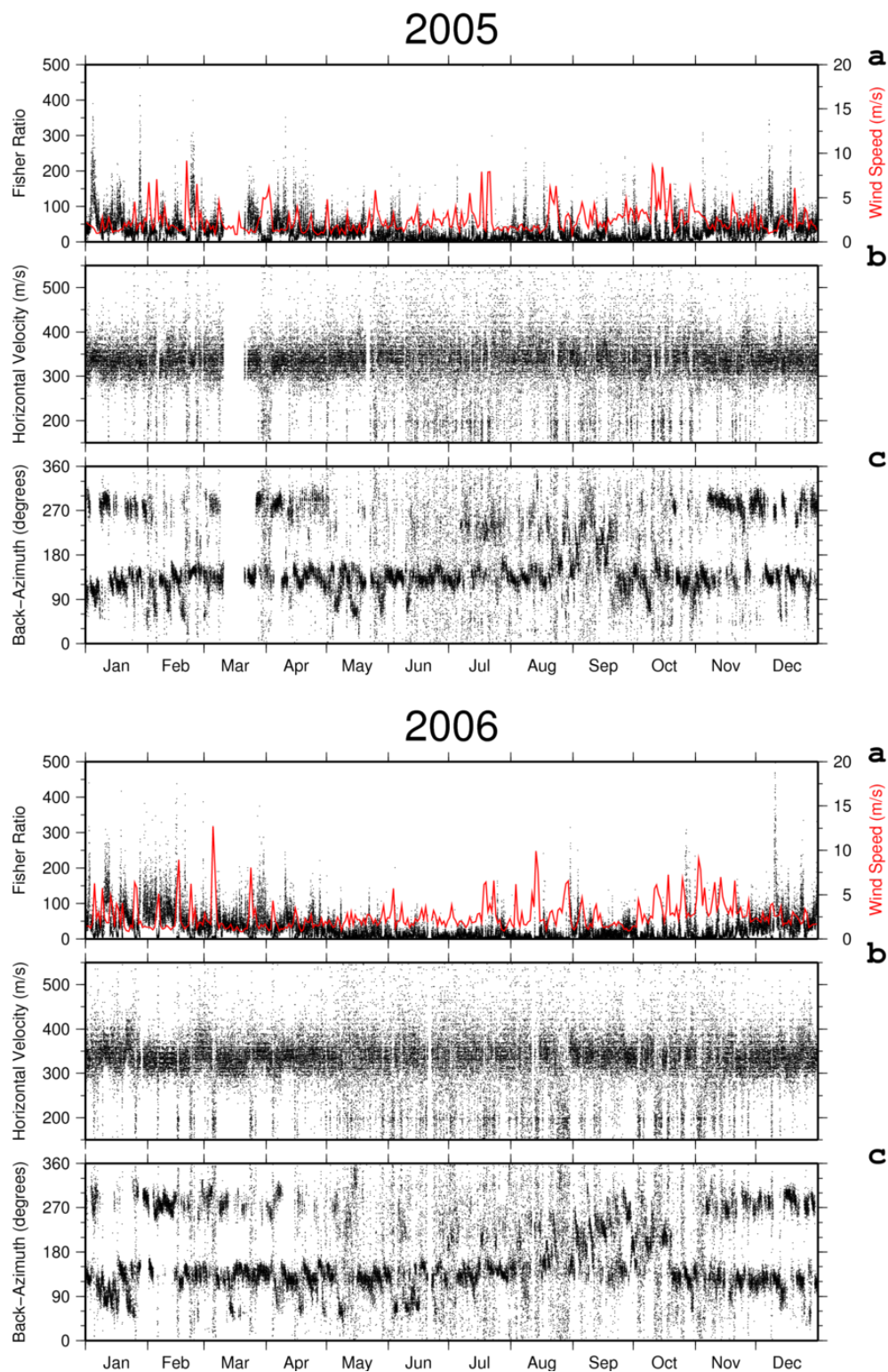


Figure 3.3: Processing results for 2005 & 2006. Frames **a** present the Fisher ratios. In the same frames, the wind speed is indicated by the red line. Frames **b** and **c** show the corresponding horizontal velocities and back-azimuths respectively. A gap in the infrasound data is present halfway March, 2005.

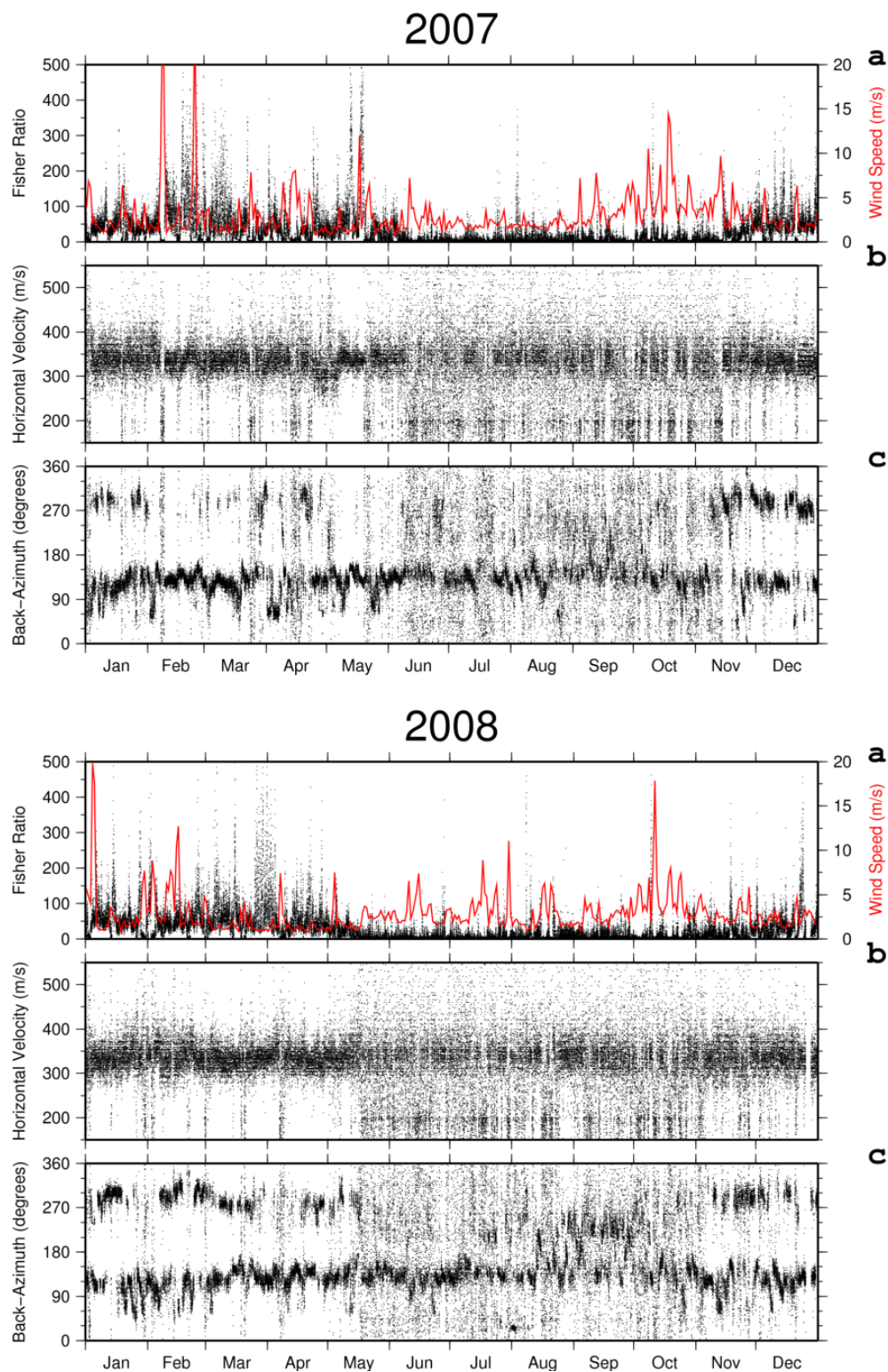


Figure 3.4: Processing results for 2007 & 2008. Frames **a** present the Fisher ratios. In the same frames, the wind speed is indicated by the red line. Frames **b** and **c** show the corresponding horizontal velocities and back-azimuths respectively.

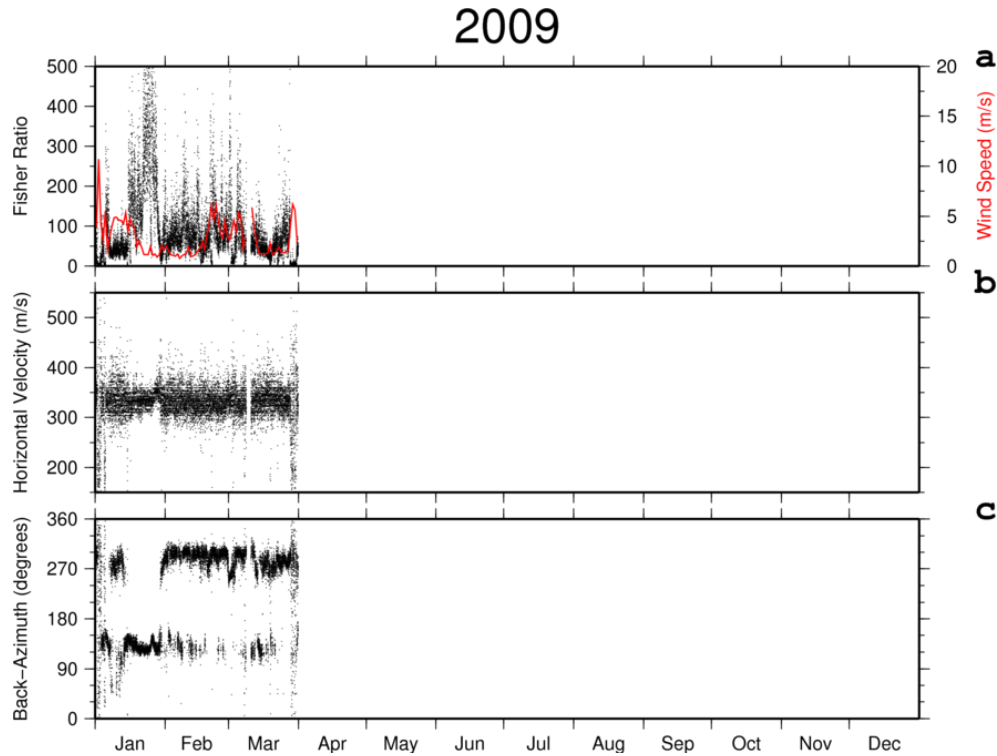


Figure 3.5: Processing results for 2009. Frame **a** presents the Fisher ratios. In the same frame the wind speed is indicated by the red line. Frame **b** and **c** show the corresponding horizontal velocities and back-azimuths respectively.

any lower Fisher ratios. The color represents the number of events detected from a certain direction at that moment in time. Where 'certain direction' and 'that moment' represent two dimensional bins of 2° in width and 3 days in length. For a better representation of the data, the scale is limited to a maximum of 10 detected events (counts in Figure 3.6). The maximum number of events detected in a single bin is 185 for 24, 25 and 26 December 2008 from a direction of $136.0^\circ - 138.0^\circ$.

Striking is the consistency of the signals recorded from the direction $120^\circ - 150^\circ$, so from the southeast. Second important back-azimuth range is the one around 280° . The correlated energy from this direction is not strong enough to interfere with the continuous infrasound from the $120^\circ - 150^\circ$ direction during summer time. However, during winter and early spring the number of signals detected from this direction exceeds the number of events with a back-azimuth in the $120^\circ - 150^\circ$ range from time to time. There are transition periods, where the back-azimuths corresponding to the highest correlations partly shift to 280° and back. During the summer, the angular variation in back-azimuth is higher than during winter time, i.e. the scatter is relatively high during summer time. The just described yearly trend is persistent over the six years.

Because Figure 3.6 includes all back-azimuths, back-azimuths corresponding to detections with very low Fisher ratios are taken into account as well. A Fisher ratio of 5

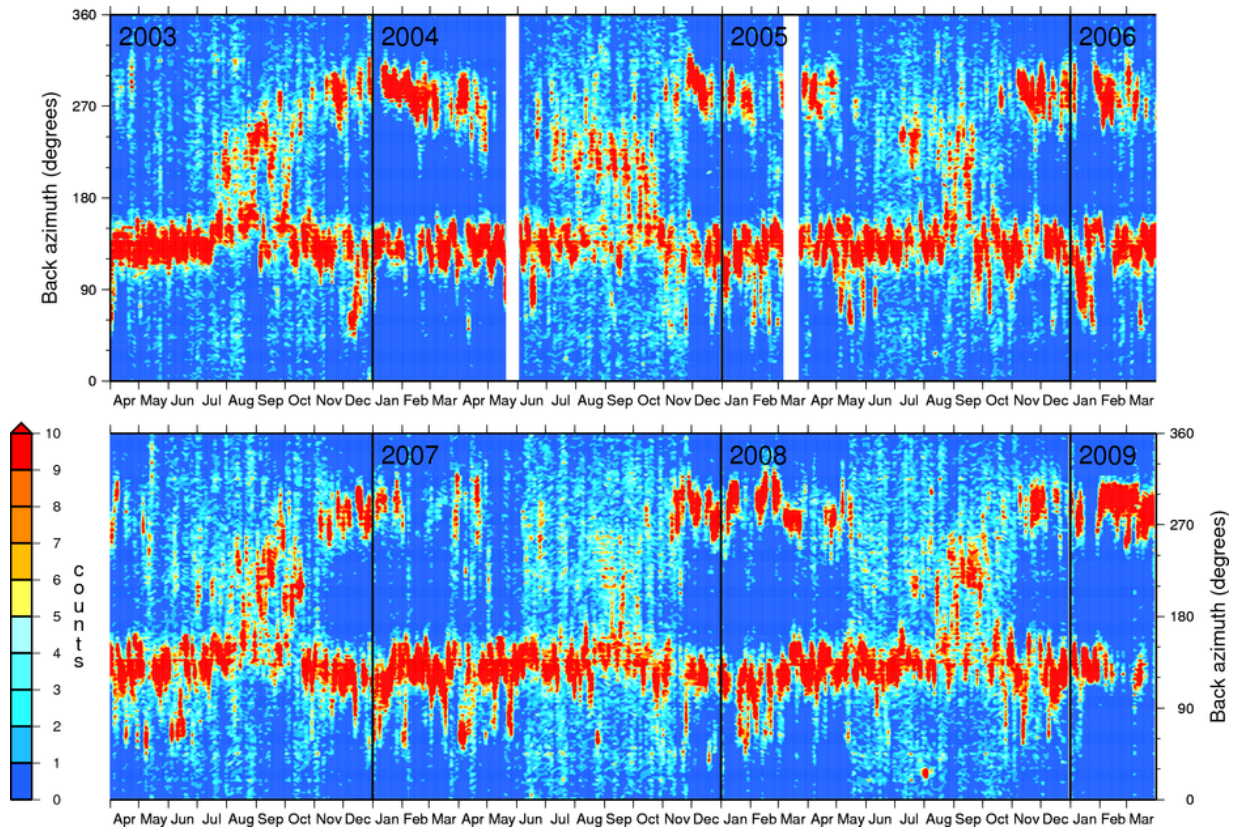


Figure 3.6: Event density versus best beam back-azimuth in the frequency range 0.1 - 1.0 Hz. The total time span ranges from March 27, 2003 till March 31, 2009. The number of detections for some of the time-angle bins overshoots the scale (note red triangle on scale). Black lines represent year limits, while the white bands are due to gaps in the data.

corresponds to a *beam-snr* of 4 for the eight stations of I18DK (see equation 2.25). This subsequently corresponds to a signal-to-noise power ratio on the traces (*snr*) of 0.5. We plot the temporal detection density with angle again with the Fisher ratio threshold set at a value of 5. The detection density of these highly correlated events is shown in Figure 3.7. The color represents the number of events detected from a certain direction at that moment in time. Where 'certain direction' and 'that moment' represent two dimensional bins of 2° in width and 3 days in length.

The total number of detections presented in Figure 3.6 is 359116. More than 78% of these detections exceed the Fisher ratio threshold of 5.0 and so a total of almost 282000 events are presented in Figure 3.7. The pattern in Figure 3.7 is only slightly differing from the pattern in Figure 3.6. The main difference is the decrease in scatter with angle during the summers. After rejecting the events having a value of F lower than 5.0, the overall trend and the two distinct bands described earlier on, remain.

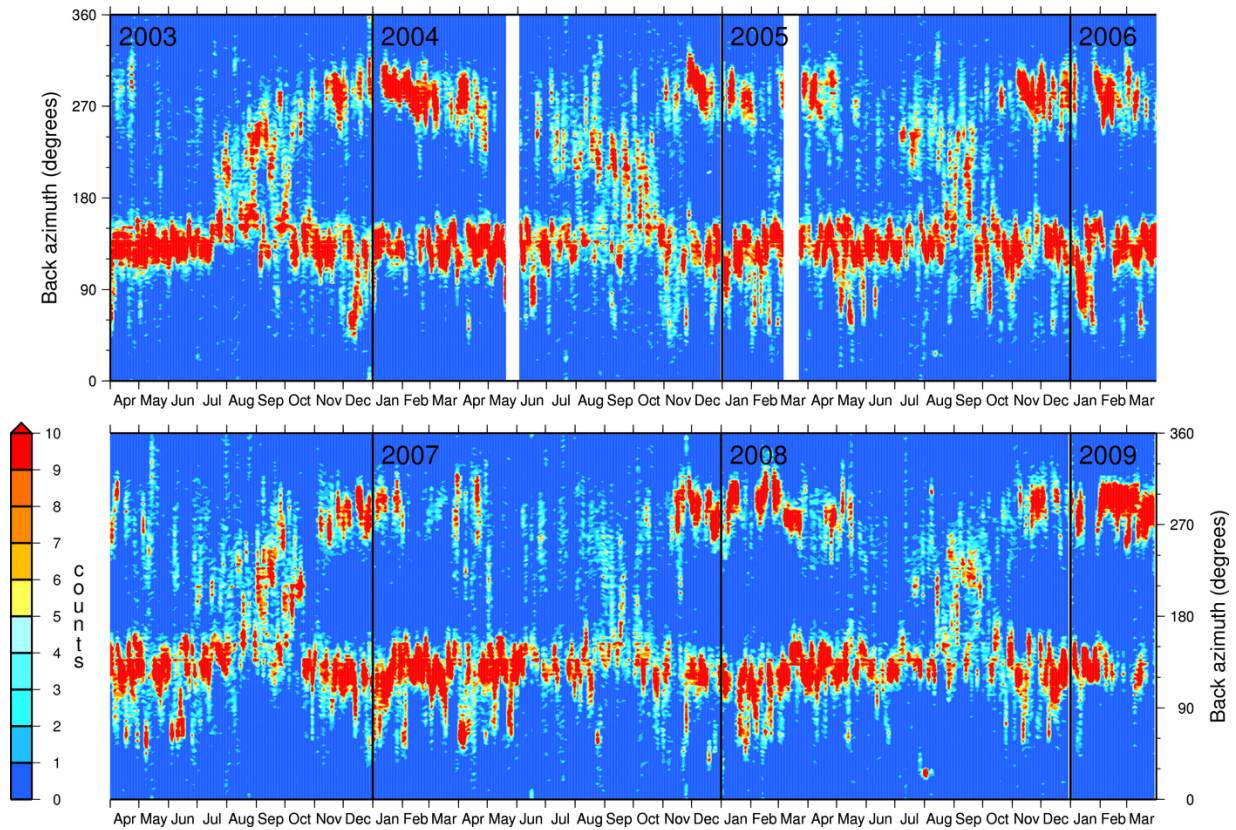


Figure 3.7: Event density versus best beam back-azimuth in the frequency range 0.1 - 1.0 Hz with the Fisher ratio threshold set at 5.0. The total time span ranges from March 27, 2003 till March 31, 2009. The number of detections for some of the time-angle bins overshoots the scale (red triangle on scale). Black lines represent year limits, while the white bands are due to gaps in the data.

Waveform

A closer look was taken at the waveforms. A strong event was taken and the waveform was examined. Figure 3.8 shows a typical event as could be observed in the 120° - 150° back-azimuth range. Figure 3.8 a shows an hour of unfiltered data for 2008-01-08, 14:00:00-15:00:00 UTC. On this time-scale only very low frequency variations can be observed. After demeaning of the data, and applying the second order Butterworth filter, Figure 3.8 b shows an enlargement of ten minutes of the data. The scale is uniform for all of the eight sensors and the maximum vertical value designated on the left side (bad visible in figure) is 0.25 Pa. Another zoom on the exact analysis window that yielded the Fisher ratio of 261 is shown in Figure 3.8 c. The maximum vertical value designated on the left side is 0.13 Pa here.

The other attributes corresponding to this time window are a horizontal velocity of 343 m/s and a back-azimuth of 126° . Giving thought to the array configuration (Figure 2.4), you can indeed observe the signal coming from the ESE direction as the two peaks

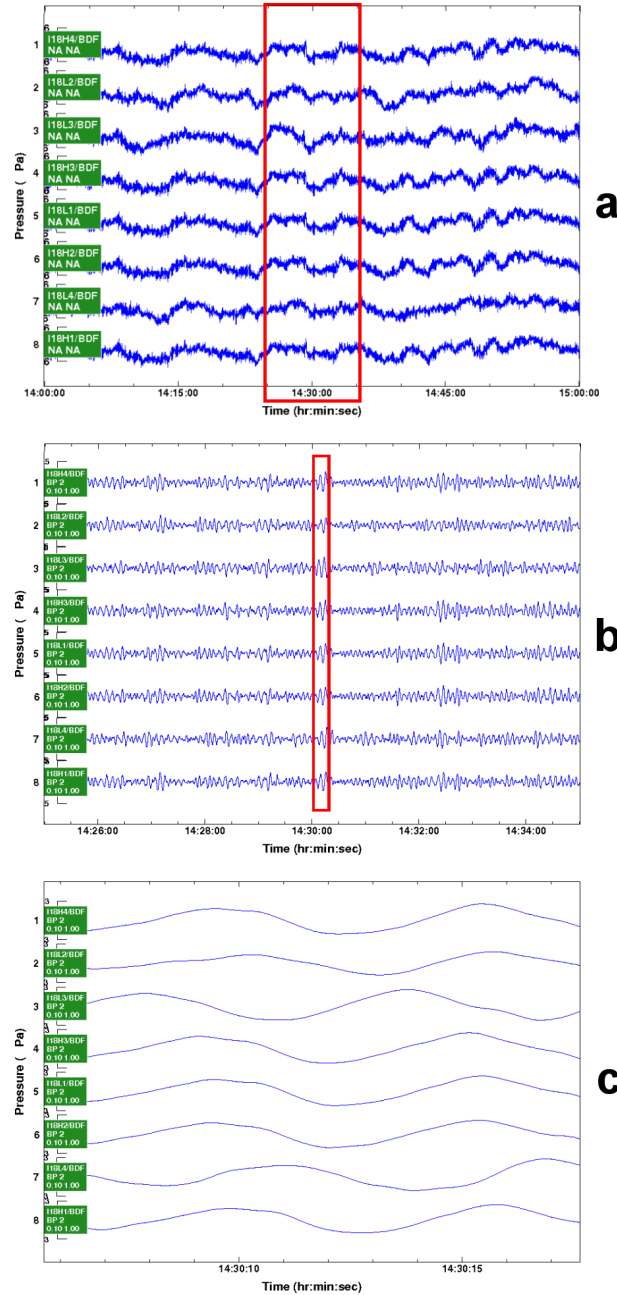


Figure 3.8: Infrasonic waveforms measured on I18DK infrasound array I18DK infrasound array on 2008-01-08. (a) Raw, unfiltered data; timespan 14:00:00-15:00:00 UTC. (b) Demeaned, 0.1 - 1.0 Hz band pass filtered (2^{nd} order Butterworth filter) time designated by the red box in (a); timespan 14:25:00-14:35:00 UTC. (c) The exact analysis window of 12.8 s on which beam-forming was applied (time window designated by the red box in b). For the demeaned and filtered data (b & c), the maximum vertical axis value is 0.25 Pa and 0.13 for (b) and (c) respectively. The variables corresponding to this specific event are: Fisher-ratio = 261, Horizontal velocity = 343 m/s and back-azimuth = 126°

within the analysis window of Figure 3.8 c can be seen on the I18L3 microbarometer first and subsequently affect the different sensors one by one to finally leave its footprint at I18L4. The period of this infrasound wave is approximately 6 seconds which means that the frequency of the signal is about 0.16 Hz.

This implicates that the uncertainty in the horizontal velocity and back-azimuth is relatively high compared to the uncertainty in these two attributes for higher frequencies. The 0.9 contour for $R(0.2, \bar{p})$ is approximately 0.001 s/m away from the maximum value of 1 for $R(0.16, 0)$ in figure 2.5. This means for this specific event (horizontal velocity of 343 m/s) that a 10% lower Fisher ratio corresponds to a velocity range of 255 - 522 m/s and a back-azimuth deviation of 20° approximately. The high Fisher ratio compensates for this array response effect however, i.e. the signal-to-noise power ratio on the traces (snr) has a value of $(261 - 1)/8 = 32.5$.

3.3 1.0 - 6.0 Hz band

Basic processing results

The processing results for the 1.0 - 6.0 Hz frequency band are presented in Figures 3.9, 3.10, 3.11 and 3.12. For each year the three calculated attributes are presented over time. For the sake of comparison, the same scales are used each year. In the top frames (**a**) the Fisher ratios are presented with the scale ranging from 0 to 25. A small number of the total number of Fisher ratios, exceeds this maximum scale value of 25. When comparing the results of the 0.1 - 1.0 band pass filtered data with the results for this frequency band, this is important to bear in mind. The wind speeds plotted in the same frame are the the daily mean wind speeds calculated from the measured wind speeds by I18DK. The middle frames (**b**) show the corresponding calculated horizontal velocities with the vertical axis ranging from 150 m/s to 550 m/s. For the purpose of a clear distinction between the different values, the rejection of few of the horizontal velocity values exceeding the 550 m/s or ducking the minimum scale value of 150 m/s is accepted. The back-azimuth values are presented in the bottom frames (**c**).

For every year can be observed that during the months July, August and September, the Fisher ratios have higher values. Overall, no Fisher ratios lower than 1.5 can be observed. Again, in the same period as observed for the lower frequency band (end of May till end of November), the scatter in the horizontal velocity values as well as for the back-azimuths is a bit higher as compared to the other part of the year. However, this increase in scatter for these two attributes shows a temporary decrease during the higher Fisher ratio period of July, August and September. This temporary decrease is not every year as distinct, especially not for the back-azimuth values.

Most detections have horizontal velocities somewhat lower than the speed of sound at the earth's surface for a temperature of 20°C , i.e. 343 m/s. That is, the distinct dark horizontal bands in the horizontal velocity plots is centered around around 320 m/s approximately. So in general, the calculated horizontal velocities are lower than those

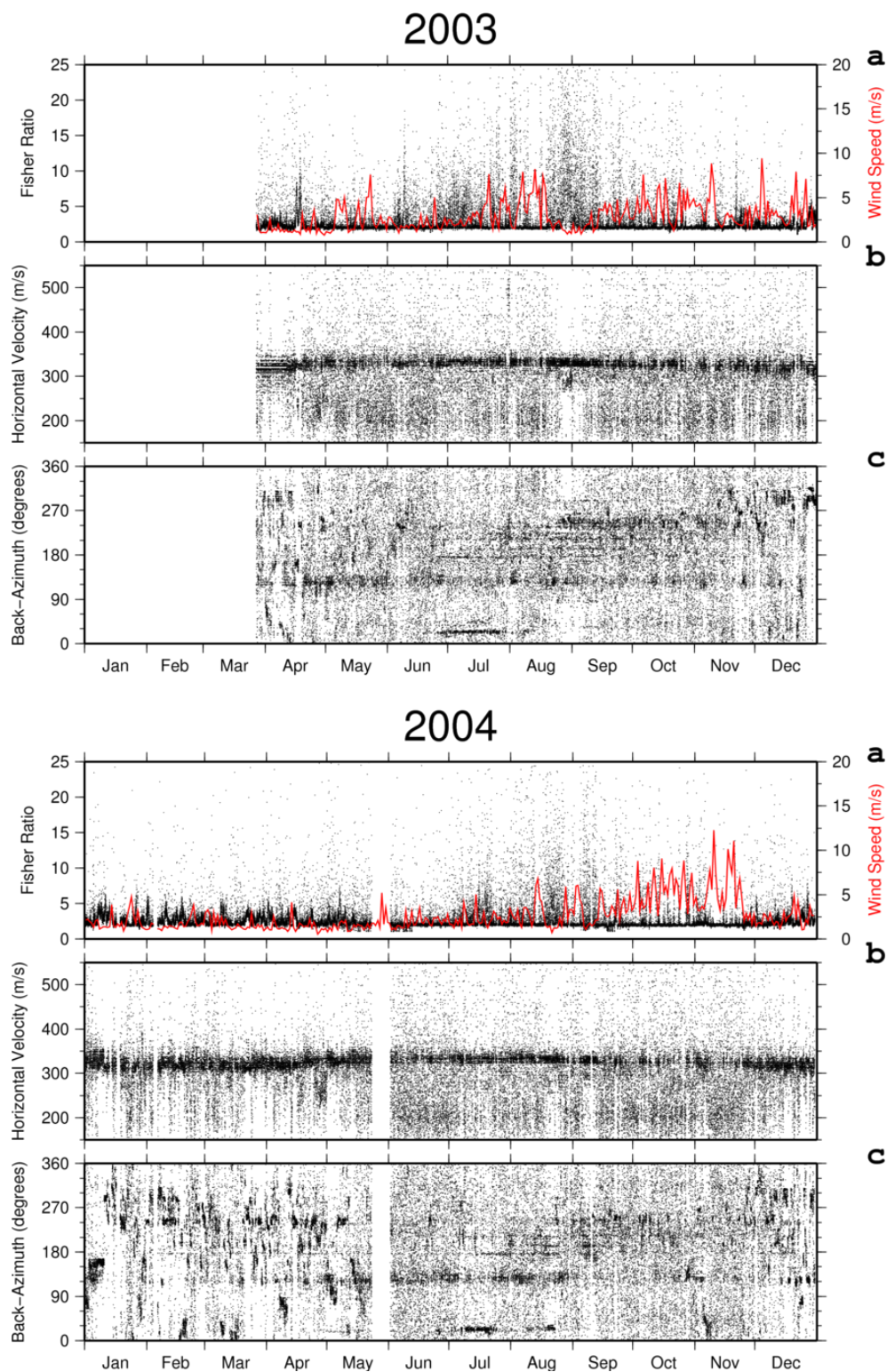


Figure 3.9: Processing results for 2003 & 2004. Frames **a** present the Fisher ratios. In the same frames, the wind speed is indicated by the red line. Frames **b** and **c** show the corresponding horizontal velocities and back-azimuths respectively. A gap in the infrasound is present at the end of May, 2004.

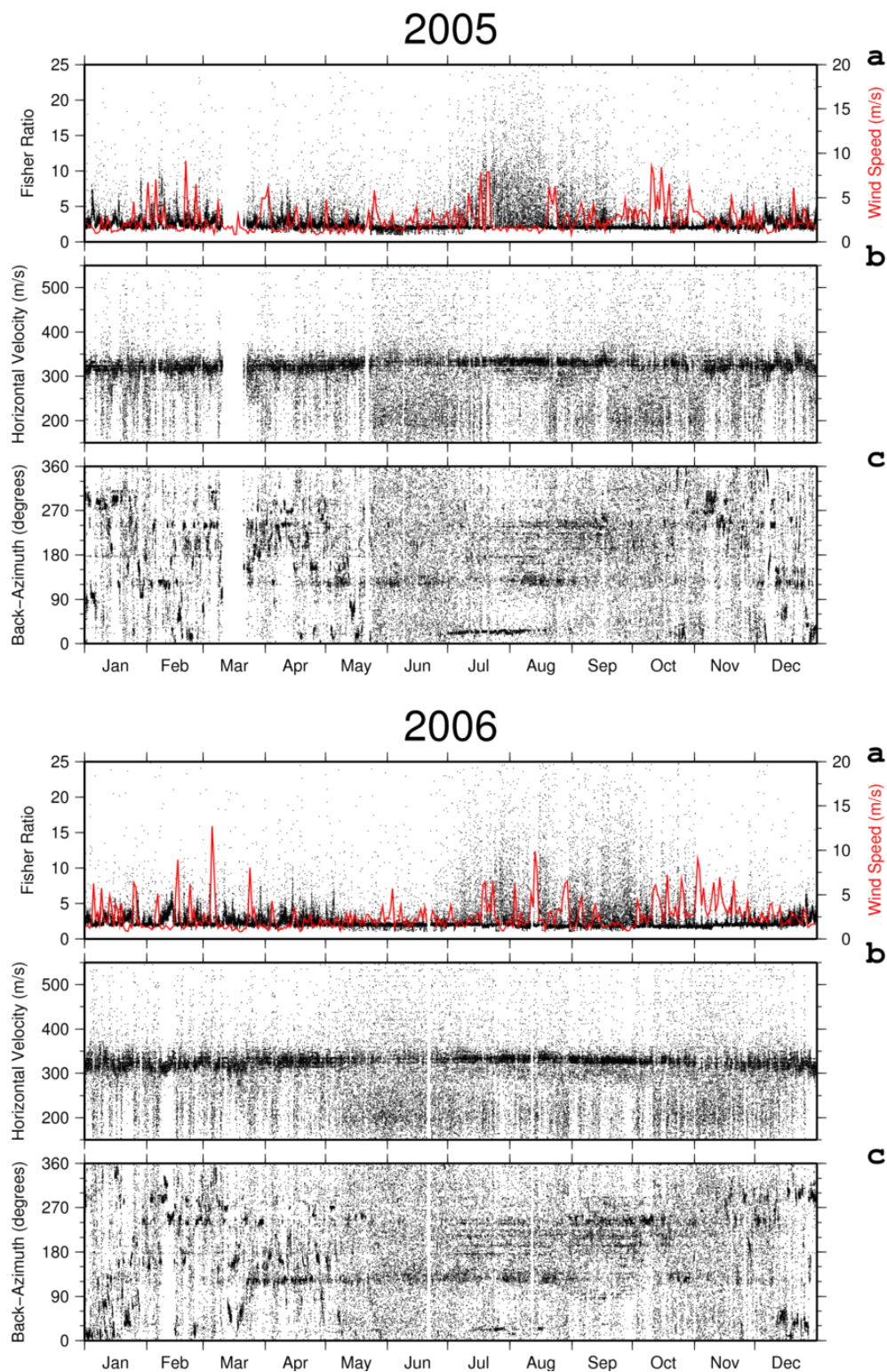


Figure 3.10: Processing results for 2005 & 2006. Frames **a** present the Fisher ratios. In the same frames, the wind speed is indicated by the red line. Frames **b** and **c** show the corresponding horizontal velocities and back-azimuths respectively. A gap in the infrasound data is present halfway March, 2005.

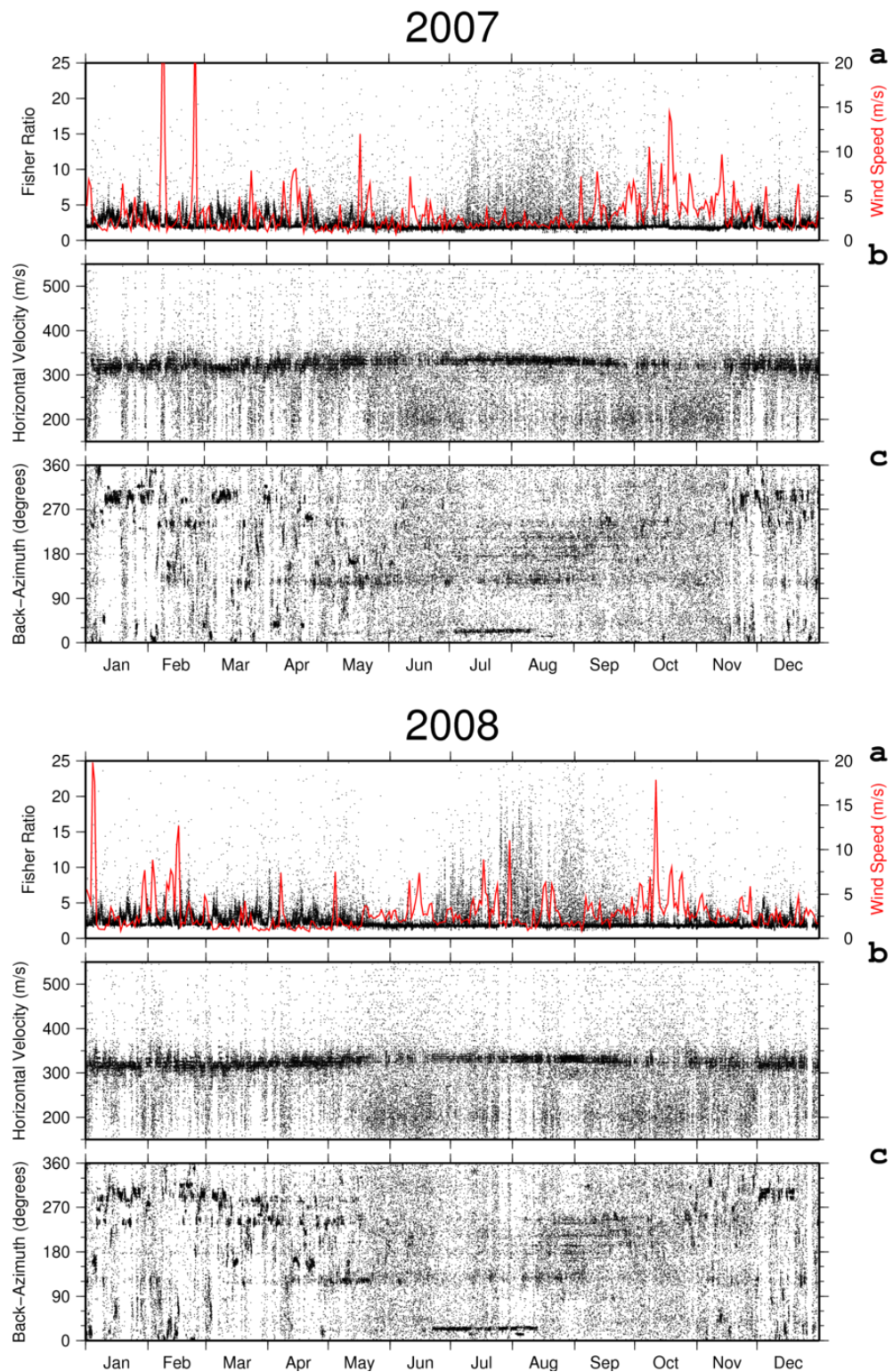


Figure 3.11: Processing results for 2007 & 2008. Frames **a** present the Fisher ratios. In the same frames, the wind speed is indicated by the red line. Frames **b** and **c** show the corresponding horizontal velocities and back-azimuths respectively.

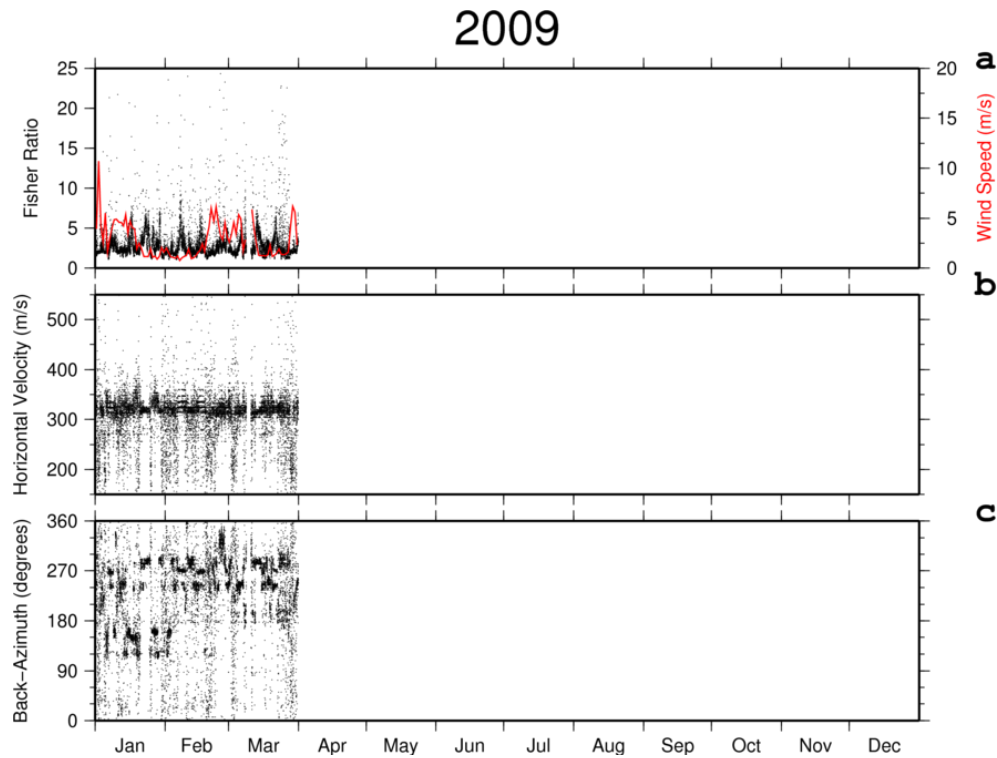


Figure 3.12: Processing results for 2009. Frame **a** presents the Fisher ratios. In the same frame the wind speed is indicated by the red line. Frame **b** and **c** show the corresponding horizontal velocities and back-azimuths respectively.

obtained by the processing of the 0.1 - 1.0 Hz band pass filtered data. Remarkable is the slight curve that can be observed in this dark band, i.e. the dense horizontal band expresses slightly higher values during summer time. This observation shall be discussed in section 4.1 of chapter 4. Furthermore, the bands are less wide as those observed in the horizontal velocity plots of the 0.1 - 1.0 Hz band. Features in the back-azimuth plots will be discussed in the section below.

Back-azimuth variation

Just as for the lower frequency band, a similar plot as Figure 3.6 has been produced for this frequency band. Again all detected events are taken into account. The bins are 2° in width and 3 days in length, just as for the lower frequency band. For a better representation of the data, the scale is limited to a maximum of 10 detected events (counts in Figure 3.13). As one can clearly see in Figure 3.13, the scatter is considerably higher than for the temporal variation of back-azimuth density with angle of the lower frequency band. The prominent range between 120° and 150° is clearly visible again. To a less extend this is also the case for events with back-azimuths close to 280° . However, some other clear features pop up in Figure 3.13 as well.

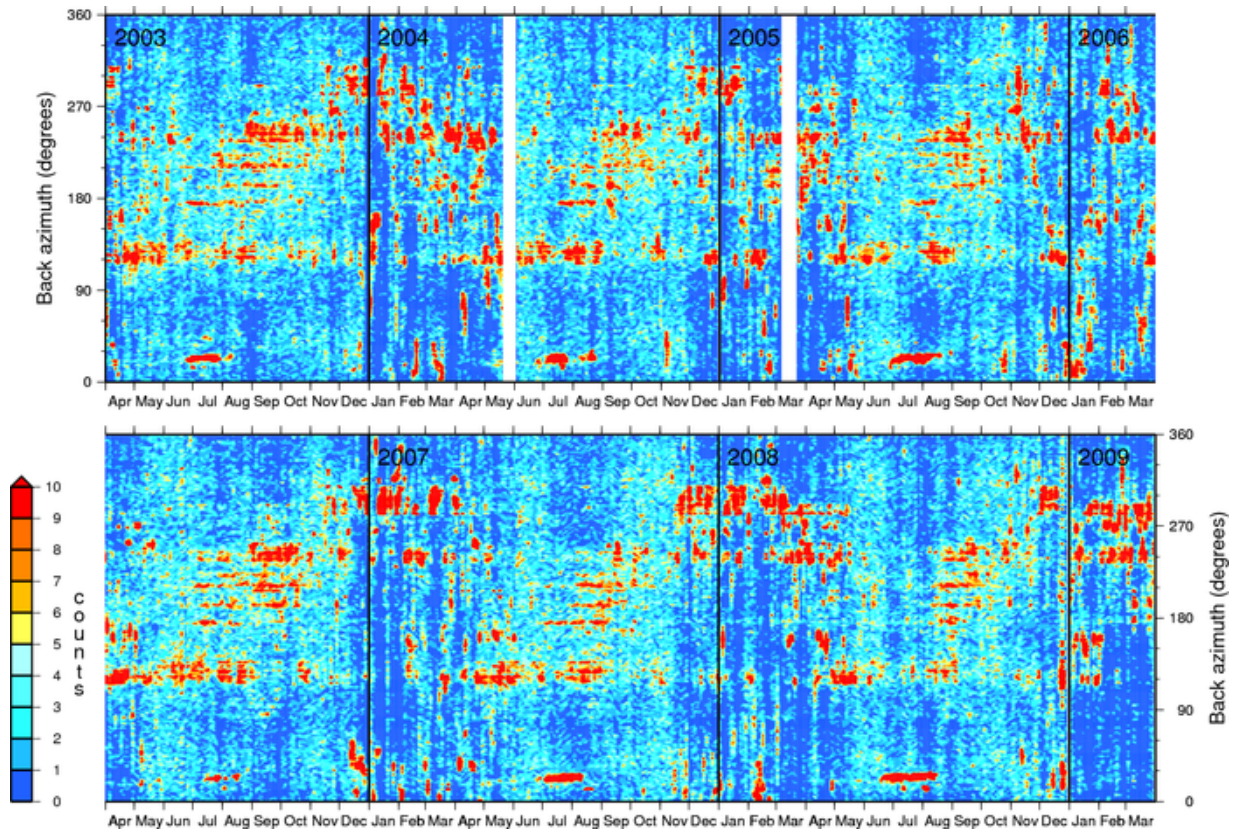


Figure 3.13: Event density versus best beam back-azimuth in the frequency range 1.0 - 6.0 Hz. The total time span ranges from March 27, 2003 till March 31, 2009. The number of detections for some of the time-angle bins overshoots the scale (red triangle on scale). Black lines represent year limits, while the white bands are due to gaps in the data.

First of all, in the lower frequency band, almost no signals are recorded coming from a northerly direction. That is, in the range of back-azimuth 330° - 40° almost no detections are visible. However, the high frequency band does show considerable detections from especially the direction of 0° - 40° . During winter time, very short periods of time (a week or less) show a high density of events originated towards that direction, while during the months July and August a high number of events is detected from a direction pointing towards 25° approximately.

Secondly, there are several narrow bands with a high event density between 150° and 240° visible during summer time. These bands can be seen clearly each summer. The band close to 180° can be observed almost continuously over the full six years, although partly concealed by the large scatter during some periods.

Just as for the low frequency band, a Fisher ratio threshold of 5.0 was set (Figure 3.14). However, in this case only about 10% of the detections exceeded this Fisher ratio threshold, so close to 36,000 events out of a total of 357,091 are presented in Figure 3.14. The comparison of Figure 3.13 and 3.14 certainly shows the impact of applying this Fisher

ratio threshold. The overall pattern in Figure 3.14 is highly differing from that in Figure 3.13 and features that are hard to observe in the former figure, pop out clearly in the latter one.

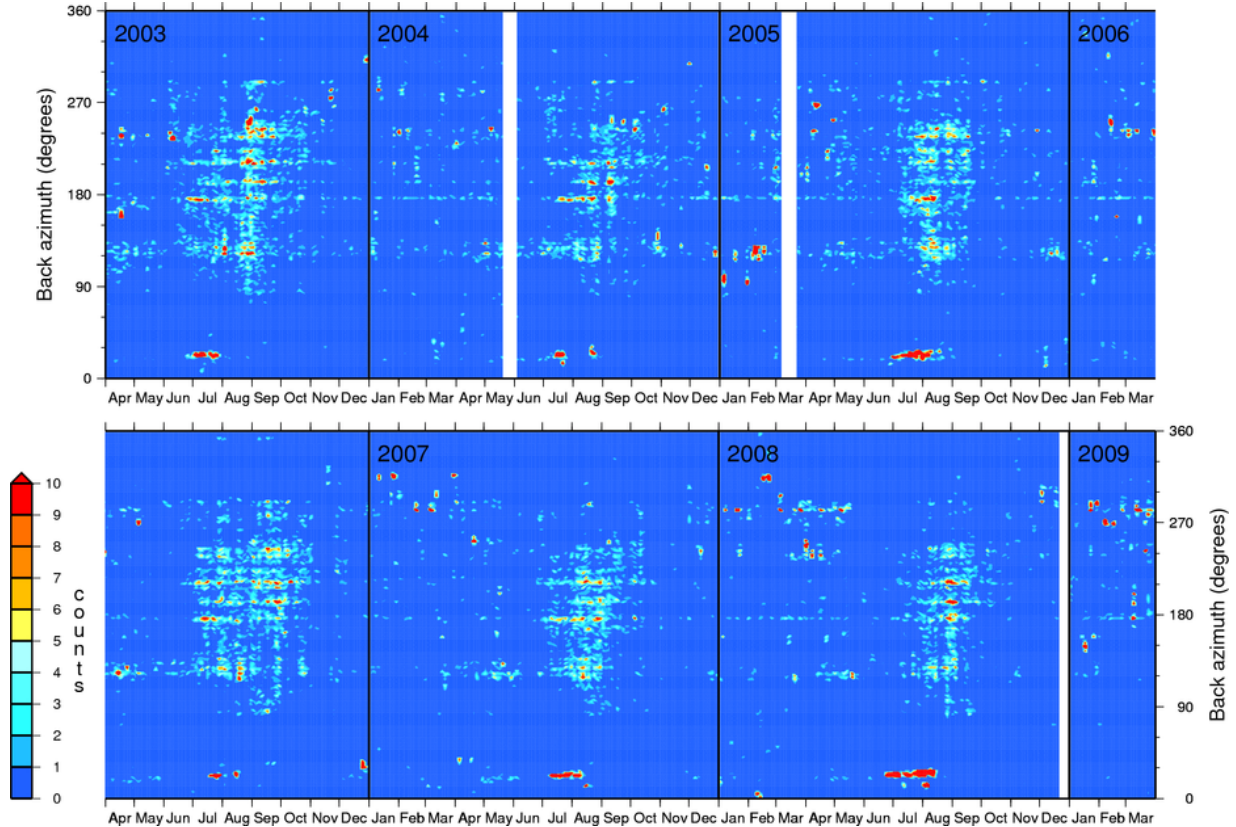


Figure 3.14: Event density versus best beam back-azimuth in the frequency range 1.0 - 6.0 Hz with the Fisher ratio threshold set at 5.0. The total time span ranges from March 27, 2003 till March 31, 2009. The number of detections for some of the time-angle bins overshoots the scale (red triangle on scale). Black lines represent year limits, while the white bands are due to gaps in the data.

There is a clear seasonal dependence of the number of events detected. In summer time, the total number of events with a high signal-to-noise power ratio is considerably higher than during the other periods of the year. Especially August and September show high densities. Except for the annual blob of events detected from a direction around 25° in July or/and August, there are almost no events having a back-azimuth between 300° and 80° . So most of the stronger events are originated south of the array. A closer look at the summer pattern of the data reveals the earlier noted narrow bands between 150° and 240° even better. Especially the earlier noted narrow band close to 180° pops out very clear. Less clear are two other narrow bands visible each summer: one around 190° and one around 212° . Furthermore, the two wider bands already observed in the 0.1 - 1.0 Hz filtered data remain visible, although discontinuous, after setting the threshold.

Waveform

A closer look was taken at the waveforms. A strong and representative signal was taken and the waveform was examined. Figure 3.15 shows a typical event as could be observed in the $174^\circ - 185^\circ$ back-azimuth range. Figure 3.15 a shows a bit more than ten minutes of unfiltered data for 2008-08-28, 00:19:45-00:30:05 UTC. The event already jumps out clearly in the traces here. After demeaning of the data and applying the second order Butterworth filter, Figure 3.15 b shows an enlargement of the red box in Figure 3.15 a. The scale is uniform for all of the eight sensors and the maximum vertical value designated on the left side (bad visible in figure) is 1.0 Pa. Another zoom on the exact analysis that yielded the event Fisher ratio of 72 is shown in Figure c. The maximum vertical value designated on the left side is 1.0 Pa again.

The other resulting variables corresponding to the analysis window shown in Figure 3.15 are a horizontal velocity of 336 m/s and a back-azimuth of 179° . Giving thought to the array configuration (Figure 2.4), you can indeed observe the signal coming from the south direction as it can be seen on the I18L3 microbarometer first (7th trace) and subsequently affects the different sensors one by one to finally leave its footprint at I18L2 (3rd trace).

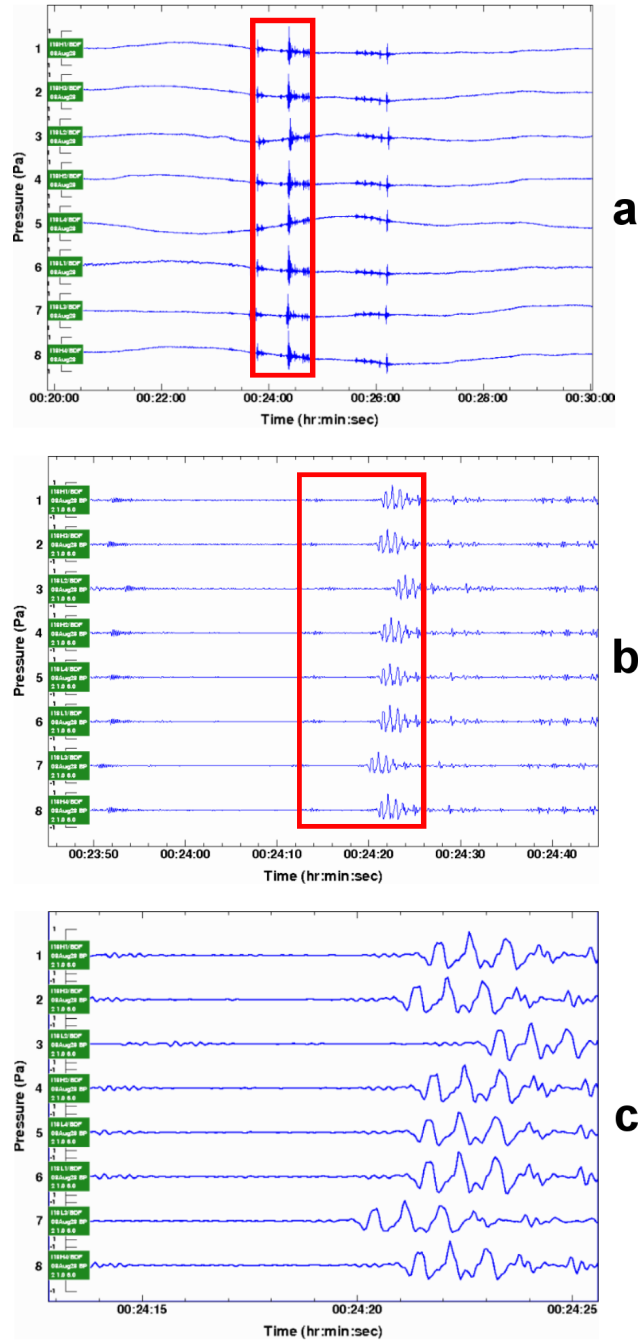


Figure 3.15: Infrasonic waveforms measured on I18DK on 2008-08-28. (a) Raw, unfiltered data; timespan 00:19:45-00:30:05 UTC. (b) Demeaned, 1.0 - 6.0 Hz zero phase band pass filtered (2^{nd} order Butterworth filter) timespan designated by the red box in (a). (c) The exact analysis of 12.8 s on which beam-forming was applied (time window designated by the red box in **b**). For the demeaned and filtered data (**b** & **c**), the maximum vertical axis values are 1.0 Pa. The variables corresponding to this specific event are: Fisher-ratio = 72, Horizontal velocity = 336 m/s and back-azimuth = 179°

Chapter 4

Interpretation & Discussion

4.1 Local weather dependence

Several studies already addressed the influence of local weather conditions on infrasound data [*Woodward et al. (1994)*; *Bowman (2005)*]. In general, the ambient noise at infrasound stations is highly variable by season, time of day and station. For an individual station, noise spectra may vary by four orders of magnitude at any frequency [*Bowman (2005)*].

Wind dependency

The variability in noise spectra described by, among others *Bowman (2005)* is mainly caused by the variability in local wind speed. The relationship between wind and infrasonic noise is given by Bernoulli's equation for an incompressible steady non-viscous flow:

$$p + (\rho v^2)/2 + \rho gh = C \quad (4.1)$$

where p is the pressure, ρ the mass density, v the wind speed, g the gravitational acceleration, h the height and C is a constant. If energy is conserved and g and h are held constant, i.e. a horizontal wind vector, the velocity and pressure are inversely related. Because ρ is constant as well (incompressible flow), simply taking the derivative of equation 4.1 shows that:

$$\delta p = -\rho v \delta v \quad (4.2)$$

This means that a higher variability in wind speed relates to a higher variability in pressure.

At a spacing of 10's of meters wind noise is known to be incoherent [*Priestley (1966)*]. The microbarometers of I18DK are spaced more than 100 meters apart. According to the relation between the variability in wind speed and the variability in pressure, one would expect the Fisher ratio's to go down for periods with stronger gusts, as these stronger gusts would increase the uncorrelated noise levels.

A quick inspection of the basic processing results in chapter 3, indeed strongly suggest a relation between the detected Fisher ratios and the wind speed at the station site. This is confirmed by zooming in. The red graph in Figure 4.1 gives the hourly mean wind speed

for October 2007. Periods of high wind speeds actually are periods with stronger gusts. The processing results in the 0.1 - 1.0 Hz band for this month clearly show that these periods correlate with periods having low Fisher ratios. Consider for example the three subsequent windy periods around October, 8, 14 and 19 and verify the coinciding drop in Fisher ratios and increase in scatter of the two other attributes (Figure 4.1 **b** and **c**). Even so, at the end of the 10th day, the atmosphere is very calm at ground level and the detected Fisher ratios increase to values of almost 300.

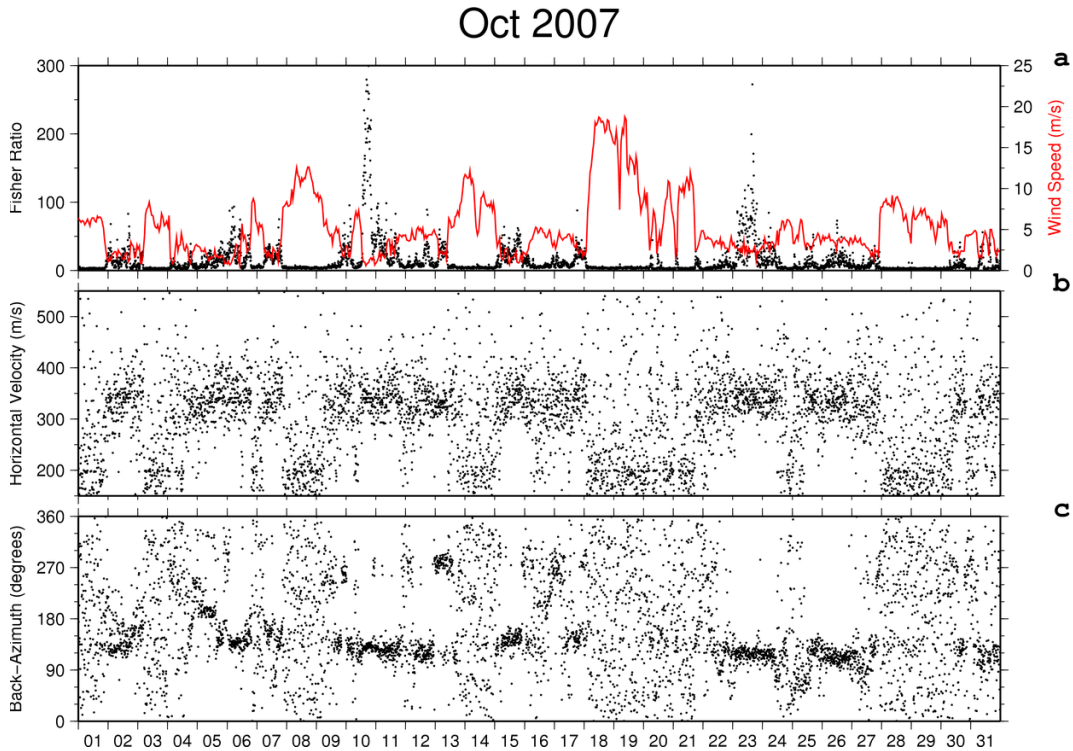


Figure 4.1: Fisher ratios (**a**), horizontal velocities (**b**) and back-azimuths (**c**) for October 2007 for the frequency band between 0.1 and 1.0 Hz. On the horizontal axis, the days of the month are given. Hourly mean wind speed at the station site is given by the red graph in **a**.

From the processing results in chapter 3, it also becomes clear that, in general, the mean wind speed graphs are lower and less jagged during summer time. Figure 4.2 shows a cyclicity that can be observed to a less extent for the other years as well. Namely, that during summer time (July and August especially) there is a daily trend in the wind speed and in the detected Fisher ratios. This figure shows the processing results and wind speed for July, 2007. Every day around 20:00:00 UTC (local time 16:00:00), the wind speed peaks, leading to relatively low Fisher ratios. This is expressed by the increased scatter in horizontal velocity (**b**) and back-azimuth (**c**) as well. The phenomenon and its effects are especially well visible in the second week.

The Atmospheric Boundary Layer (ABL) is the air layer near the ground affected by diurnal heat, moisture or momentum transfer to or from the earth's surface. In general, the

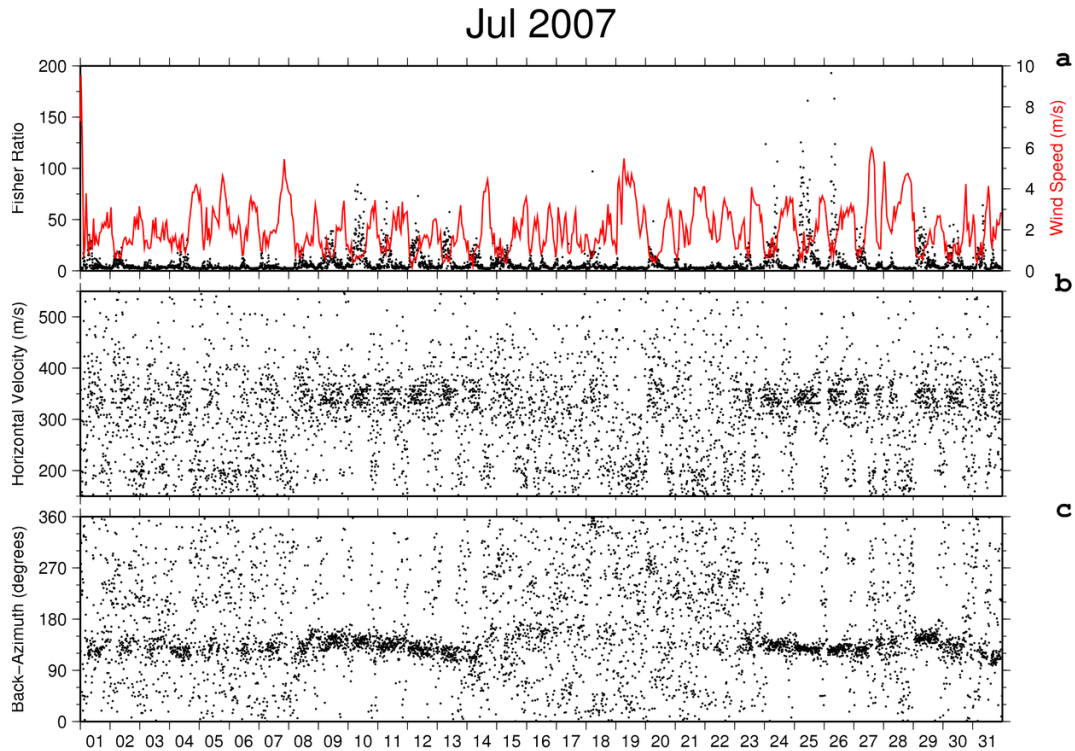


Figure 4.2: Fisher ratios (a), horizontal velocities (b) and back-azimuths (c) for July 2007 for the frequency band between 0.1 and 1.0 Hz. On the horizontal axis, the days of the month are given. Hourly mean wind speed at the station site is given by the red graph in (a).

ABL has its highest extend during the day (1 to 2 km) when the Earth’s surface radiates heat. Its lowest extend is reached during the night when its upper surface is only tens of meters above the earth’s surface or it is even nonexistent [*Kaimal and Finnigan (1994)*].

Diurnal cycles in the stability of the boundary layer have been found for the months July and August by *Cohen et al. (2007)* for the location of Summit, Greenland. *Cullen and Steffen (2001)* also showed that, for the entire Greenland ice sheet, unstable conditions occurred during the summer months (June 1, October 15) for 1998, 1999, and 2000, respectively. Figure 4.2 makes one expect that the same destabilization occurs at the edges of the Greenland ice cap as well. *Evers and Schweitzer (2010)* find the same diurnal variability in Fisher ratios for the ARCES infrasound array in Norway as we find for I18DK.

In Thule the increased power of the sun during daytime causes destabilization concentrated in the ABL. Although the sun never sets in Thule during summer time, a more stable boundary layer when the sun is close the horizon, yields less loss of coherency of infrasound signals. For this reason, the diurnal destabilization of the boundary layer, corresponding to an increased turbulence of the air just above the surface, most likely is the cause for the diurnal variations in mean hourly wind speed and Fisher ratios seen in Figure 4.2. During wintertime the sun is absent and so is the diurnal variation.

Woodward et al. (1994) show the seasonal and diurnal variation of infrasound recordings

due to wind speed variations. Their most basic observation from the analysis of 22 infrasound stations is that noise at most stations increases gradually up to a certain wind speed, beyond which the noise increases more rapidly with wind speed. Figure 4.3 b presents the estimated relations between RMS micropressure in the 1.0-2.0 Hz band and the mean wind speed for nine different stations. This is done for October 2004, using data windows of 10 minutes with 50% overlap between consecutive windows. Regression is subsequently applied to obtain the relation curves. The level of affection by microbaroms, i.e. variation in source strength, causes the large variation at low wind speeds. For details consult *Woodward et al.* (1994).

Woodward et al. (1994) also compare the power spectra for different mean wind speeds. They have done this for several stations. In Figure 4.3 a the result is presented for station I08BO, but for I18DK they obtained a similar result. It is clear that the power spectra increase with increasing wind speed and decrease with increasing frequency of the infrasound recordings. *Bowman* (2005) shows the same dependencies on wind speed and frequency.

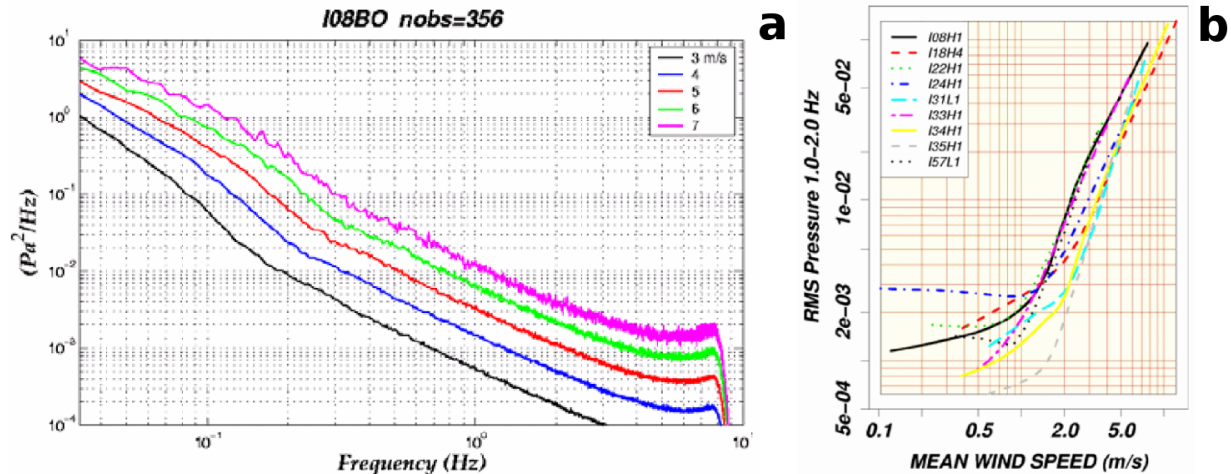


Figure 4.3: Both figures adapted from *Woodward et al.* (1994). **a:** For wind speeds ranging from 3 to 7 m/s the power spectra of I08BO are compared. *Woodward et al.* (1994) binned the power spectra of micropressure by mean wind speed. This is followed by stacking of the spectra per bin on a daily basis. It is clear that the power spectra increase with increasing wind speed and decrease with increasing frequency. They have obtained a similar result for I18DK. **b:** For nine different stations, relations between RMS micropressure (1-2 Hz) and mean wind speed are estimated for October 2004. RMS Pressure for I18H4 is given by the red dashed line.

To verify the relations stated in *Woodward et al.* (1994) qualitatively, in Figure 4.4 the raw data (trace a), 0.1-1.0 Hz filtered data (trace b) and 1.0-6.0 Hz filtered data (trace c) of microbarometer I18H4 (same sensor as shown in Figure 4.3 b) are placed one below the other. The figure shows the results together with the data from the wind speed sensor (LWS channel) (trace d). The scale is equal for all three traces with the minimum and maximum values being -100 and 100 Pa respectively. It can clearly be observed that the amplitudes decrease from the original trace to the low frequency band filtered trace and

subsequent from the low frequency band filtered trace to the 1.0 - 6.0 Hz filtered trace.

The maximum wind speed measured is just above 31 m/s around 09:00:00 UTC on October 19. The maximum absolute amplitude in the raw data corresponds to a pressure drop of almost 260 Pa (indicated by arrow in figure). This maximum absolute amplitude is probably due to a sudden extreme increase in wind speed from around 9 m/s to more than 20 m/s. In the 0.1 - 1.0 Hz filtered trace the maximum absolute amplitude has a value of a little less than 40 Pa and the higher frequency band trace shows a maximum absolute amplitude of approximately 3.85 Pa. The highest peaks are observed on October 19. In Figure 4.1 you can see that the hourly mean wind speeds on that day range from 8 m/s to more than 20 m/s.

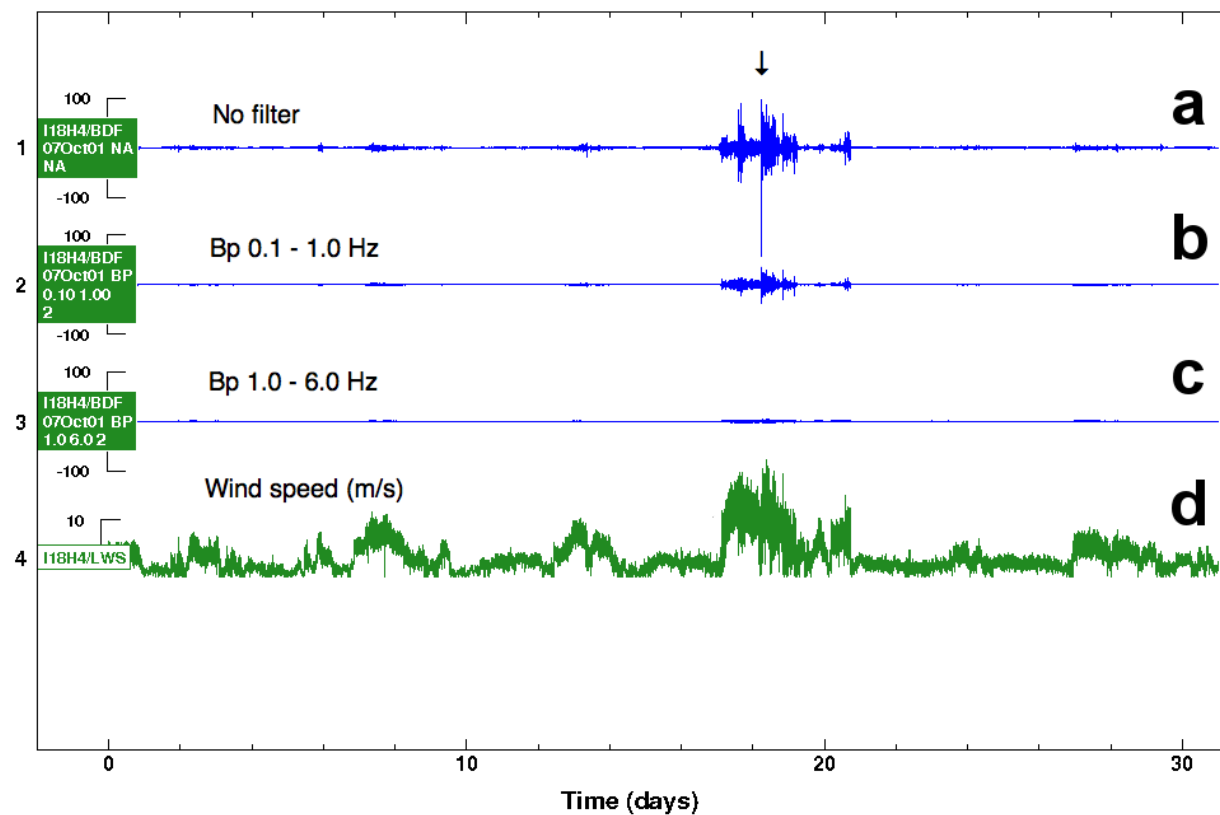


Figure 4.4: The raw data (a), 0.1-1.0 Hz filtered data (b) and 1.0-6.0 Hz filtered data (c) of microbarometer I18H4 (same sensor as shown in Figure 4.3 b) for October 2007. Wind speeds are shown by d (LWS channel). The scale is equal for all three microbarometric traces with the minimum and maximum values -100 and 100 Pa respectively.

More in-depth analysis with 'geotool' yields that the signal containing the peak close to 40 Pa in the 0.1-1.0 Hz band has a period of 10 seconds roughly. So as one would expect from Figure 4.3 a, this maximum amplitude is produced by signals acting at the lower end of the frequency band. In the same way the record containing the peak of 3.85 Pa has a period of 0.6 seconds roughly. So also this maximum amplitude is produced by noise signals acting at the lower end of the 1.0 - 6.0 Hz band, i.e. 1.67 Hz approximately.

This means that the amplitude has decreased by a factor of 10 approximately and thus the power by a factor of 100 going from 0.1 Hz to 1.67 Hz. This is less decrease as one would expect from the 7 m/s graph of Figure 4.3 a, but our observation is only a snapshot of course. Furthermore, the mean wind speed is far above of 7 m/s and it is not certain whether the graphs in Figure 4.3 have the same slopes for higher wind speeds.

Temperature dependency

The effective sound speed (equation 1.3) incorporates the temperature, wind and compositional structure of the atmosphere. We compare the theoretical speed of sound in air, i.e. C_{air} from equation 1.2 with the observed horizontal velocities of the detections in Figure 4.5. This means that the prevailing winds are not taken into account for the calculation of the theoretical sound speed, i.e. we don't use C_{eff} . Reason for this is the limitation of the wind direction channel (LWD). The wind directions measured at the station site are bounded to 280° . This problem is recognized earlier by *Bowman* (2005) for station I31KZ in Kazakhstan and he suggests an instrumentation problem is the cause.

The black graph in Figure 4.5 shows C_{air} based on the daily mean of the measured temperature. Furthermore, Figure 4.5 shows the horizontal velocities for detections in the 0.1 - 1.0 Hz band with a Fisher ratio > 10 (red) and Fisher ratio > 3 (green) and in the 1.0 - 6.0 Hz band with a Fisher ratio > 3 (blue). The daily mean temperatures were calculated for the whole year using the measurements of the temperature channel of I18DK. The four graphs were subsequently filtered using a low pass filter allowing periods exceeding 30 days.

A trade-off exists between the Fisher threshold applied and number of detections available to calculate the daily mean horizontal velocities. In the same way a secondary trade off exists between the minimum number of the detections required to calculate a daily mean and the significance of the mean. Playing around with these thresholds and required minimum number of detections yielded the values used to produce Figure 4.5. Taking a Fisher ratio higher than three as threshold would eliminate too many detections, to plot a reliable graph in the 1.0 - 6.0 Hz range. The daily means of the detected velocities are calculated in case there are more than 5 detections exceeding the Fisher threshold on that day. If that was not the case, the daily mean for that day was based on linear interpolation of the mean horizontal velocity of the day before and the day after.

The three detection velocity graphs depend highly upon the local wind speed and direction. It is difficult to attribute specific variables as causal for specific peaks of these three peaks. To a first order, the angle of incidences determines the horizontal velocity, i.e. larger θ 's correspond to higher horizontal velocities of the incoming signals. Superimposed on this effect, is the combined effect of local wind conditions and prevailing source directions.

The difference between the two graphs for the low frequency band detections (red & green) is remarkable. The one including all detections with Fisher ratios higher than 3 (green) approaches the graph for the 1.0 - 6.0 Hz band detections during some summer and fall periods. This is most clear for 2006 and 2008. This is probably due to the fact that the Fisher ratio's are relatively low for the lower frequency band during summer time.

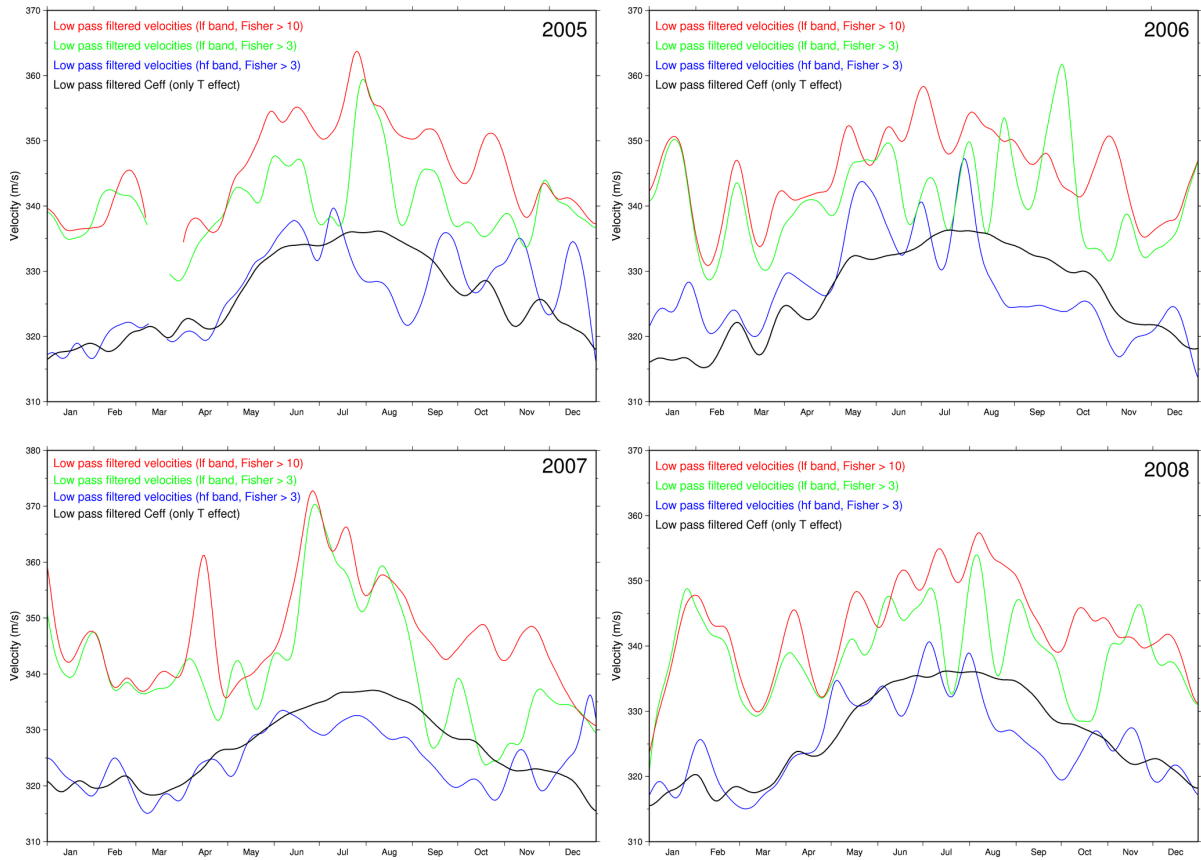


Figure 4.5: C_{air} (black), horizontal velocities of the detections with a Fisher ratio > 10 for the 0.1 - 1.0 Hz filtered data (red), horizontal velocities of the detections with a Fisher ratio > 3 for the 0.1 - 1.0 Hz filtered data (green) and horizontal velocities of the detections with a Fisher ratio > 3 for the 1.0 - 6.0 Hz filtered data set (blue). C_{air} values are calculated from daily mean temperatures as measured by the station thermometer of I18DK using equation 1.2. To all four graphs, a low pass filter with a corner frequency corresponding to a period of one month is applied.

The number of signals having back-azimuths in one of the two prevailing back-azimuth ranges decreases during summer and early fall (see Figure 3.7). In the same period the Fisher ratios in the 0.1 - 1.0 Hz band have lower values. So the higher horizontal velocities correspond probably correspond to the events with higher Fisher ratios. Likely, the higher Fisher ratios subsequently correspond to the detections from $120^\circ - 150^\circ$ and those around 180° . The weaker detections from the south have the highest Fisher ratios for this period. Either a prevailing wind from the north during this period or a smaller θ of the infrasound waves corresponding to the southern sources would explain the decrease.

The number of strong signals detected in the 1.0 - 6.0 Hz data is far more numerous during summer time. During the rest of the year there is not really a prevailing source direction as you can see in Figure 3.14, but during summer and early fall by far the most

detections are originated south of the array. The blue graph shows a lower horizontal velocity than the values for C_{air} predict. This cannot lead to an other conclusion than that during August and September the prevailing wind vector is opposing the prevailing propagation vectors, i.e. during this period the prevailing wind direction is roughly north to south at the station site.

4.2 Microbaroms

Microbaroms are observed worldwide with frequencies of 0.1 - 0.4 Hz. Addressing the characteristics of these microbaroms concerning I18DK thus means that only the 0.1 - 1.0 Hz band results are discussed. The fact that the Fisher ratio's are relatively low in this frequency band during summer time cannot be explained by more noise due to high local wind speeds in summer time (see Figures 3.2 a, 3.3 a and 3.4 a). Furthermore, there is a seasonal variation in the resolved back-azimuths of the 0.1 -1.0 Hz band filtered data. Either a combination of the source and the medium or one of them independent is responsible for these seasonal variations. We shall address how and to which degree these two contributors effect the results of the analysis for the lower frequency band.

Medium dependency

Figure 4.6 shows the daily mean wind direction for an altitude of 50 km superimposed as black dots on the resolved back-azimuths of the detections with Fisher ratios higher than 5.0, i.e. these wind directions superimposed on Figure 3.6. These wind back-azimuths are calculated from the ECMWF atmospheric models described and explained in the introduction (see Figure 1.4). The wind direction is analyzed at 76.5°N, 291.5°E, which is approximately 100 km south of the location of I18DK. This is the node in the ECMWF grid closest to Thule.

It is clear from Figure 4.6 that the dominant back-azimuth of the low frequency detections is guided by the wind direction at upper stratospheric levels. During spring and fall the reversal of the polar vortex is clear. When the upper stratospheric winds blow to the west, from the start of May till the end of August, almost no strong coherent energy is detected from the west. At least not strong enough to overpower the signals from the southeast. During winter time there is still a lot of coherent energy detected from a south-east direction, contrary to one's expectations based upon the stratospheric wind direction. As we will discuss later, this probably a source effect.

Source regions

Based on their analysis of 21 globally distributed infrasound arrays, *Bowman et al.* (2005) suggest, that the power of the microbaroms is higher during winter in each hemisphere. They argue that this is due to the presence of larger storms over the oceans during winter time. This seasonal variation in the maximum power of the generated microbaroms

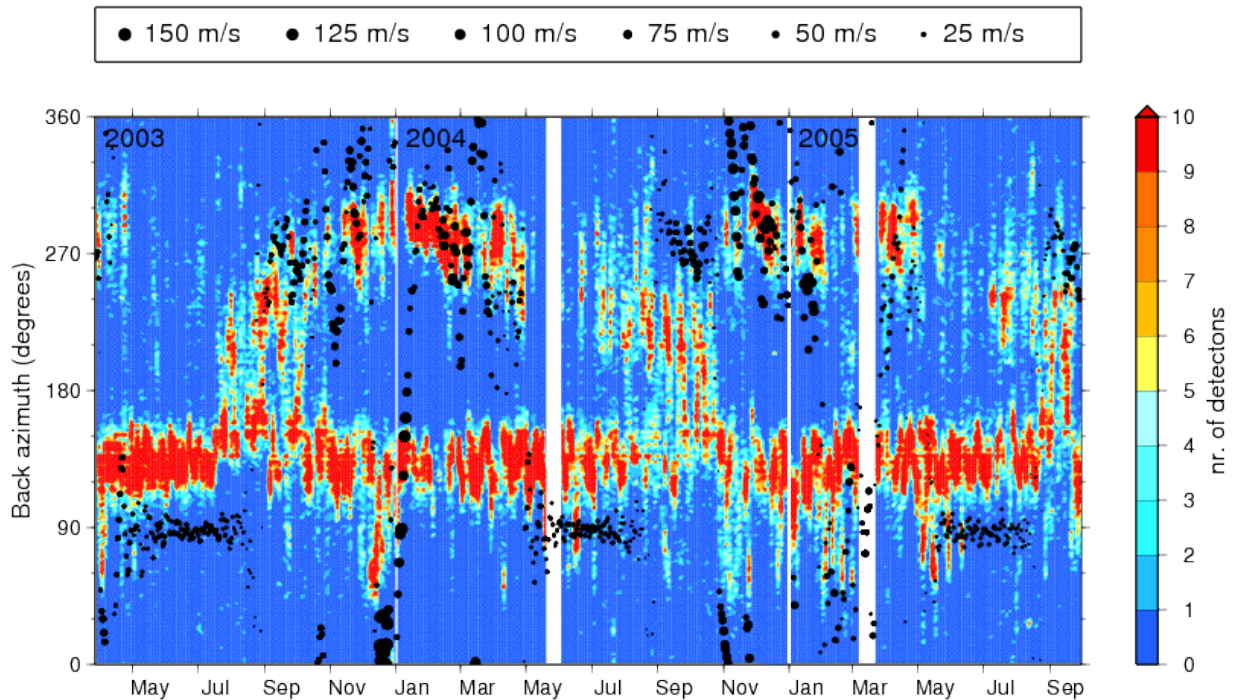


Figure 4.6: The daily mean wind direction for an altitude of 50 km superimposed as black dots on the resolved back-azimuths of the low frequency band. The surface area of the black dots is linearly scaled with the corresponding daily mean wind speed. Strongest winds are measured at the end of December, 2003, where they reach velocities over 150 m/s. The total time span ranges from March 27, 2003 till September 29, 2005. See caption of Figure 3.7 for details concerning the back-azimuth density. The white bands are due to gaps in the infrasound data.

is confirmed by a quick but efficient analysis of *Evers and Schweitzer (2010)*. From March 2008 till May 2009, they square the multiplication of the wave height and period and take this as an indicator for the source intensities. The wave heights and periods they use, are based upon oceanic wave models of the ECMWF provided at each 0.5×0.5 degree. The maximum intensity is higher during the winter period than in summer. This explains the lower Fisher ratios observed during summer time.

To better oversee the directionality of the sources in the low frequency band, all the resolved back-azimuths (six years, no Fisher ratio threshold is applied) are binned in wedges of three degrees. Originating from the station location, great circle arcs point in the direction of the center values of the back-azimuth bins and the lengths of these arcs corresponds to the number of detections falling in the bins (Figure 4.7). The microbaroms generated on the Atlantic Ocean prevail over those generated on the Pacific Ocean and the great circle arc running over the southern tip of Greenland points to the most intensive source.

Kedar et al. (2008) produced sophisticated wave-wave interaction maps for the northern hemisphere. These maps show the distribution over the oceans of regions that are more likely to generate microbaroms and microseisms in particular. Figure 4.8 consists of two figures. The bottom figure is obtained from *Kedar et al. (2008)* and shows the wave-

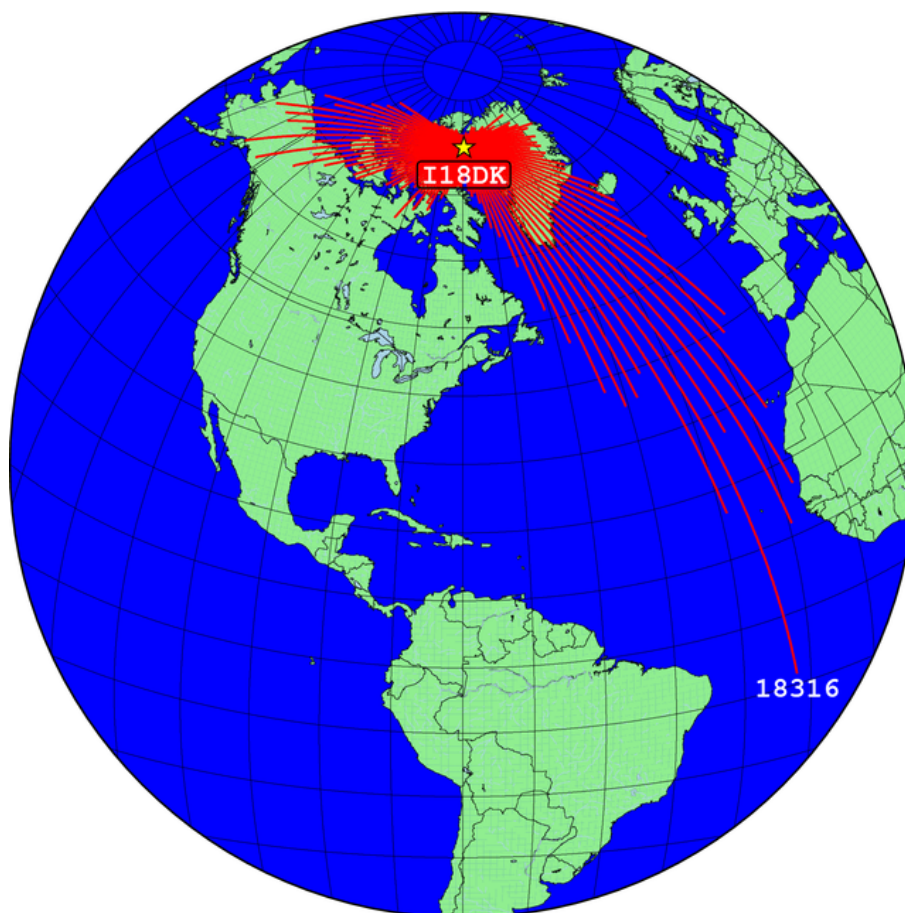


Figure 4.7: Back-azimuth domain divided in wedges of 3° . For every wedge, the total number of detected events over the full six years is calculated. The lengths of great circle arcs are scaled with respect to the great circle arc corresponding to the highest number of events detected, which in this case is the great circle arc pointing in the direction of 133.5° (range $132^\circ - 135^\circ$). 18316 events are originated to this direction.

wave interaction intensity over the oceans of the northern hemisphere for November 2003. The Atlantic Ocean is dominated by intense regions of wave-wave interaction whereas the intensity is somewhat lower and more diffuse in the Pacific Ocean. The top figure is again the earth with great circle arcs originating from the I18DK location. A sliding window of width 4° with step size 2° is used, so 180 great circle arcs are plotted. All events of November 2003 are taken into account.

There is a high coincidence between the top figure and the bottom figure. The longest great circle arcs pointing in a western direction, point exactly to the east-west aligned region of high intensity in the Pacific Ocean. Moreover, we can distinguish between the two regions of intensive wave-wave interaction in the North Atlantic Ocean. A slight dip of 8° separates the longest great circle arc (corresponding to 349 detections) from the the two long great circle arcs pointing to the north-south elongated region in the Atlantic Ocean.

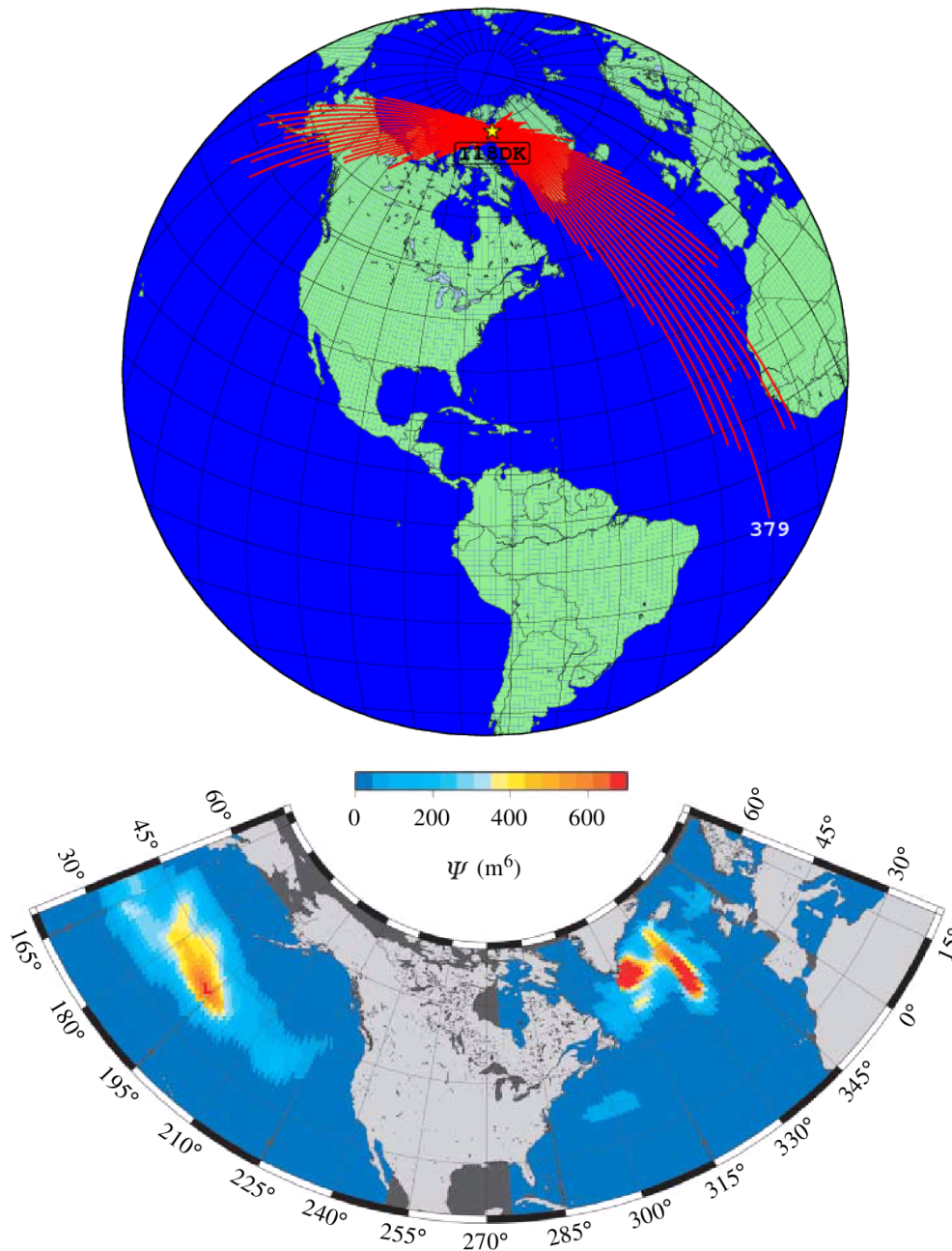


Figure 4.8: The top figure shows great circle arcs originating from the I18DK location, which lengths correspond to the number of detections within a range of 4° centered around the back-azimuth the great circle arcs point to. The bottom map shows high wave-wave interaction intensity regions derived from Wave Action Models (WAM) in the North Atlantic and North Pacific oceans. The wave-wave interaction intensity (Ψ) is averaged over the month of November 2003, for wave periods of 6 to 14 s. Figure obtained from *Kedar et al.* (2008).

The longest great circle arc points to the center of the intensive wave-wave interaction region just southeast of the southern tip of Greenland.

With the knowledge of the location of these two source regions, a note must be made on our earlier statement concerning the medium dependency. We did not expect a lot of coherent energy from a southeast direction during winter time. This was based upon the stratospheric wind direction only. However, the infrasound waves lose energy due to attenuation as they travel through the atmosphere. The source region at the southern tip of Greenland is much closer to I18DK as the source region for the Pacific microbaroms. This probably causes the continuity of the detections from 120° - 150° . Contrary to the microbaroms from the Pacific ocean, which are only detected when the stratospheric duct is better due to the stratospheric winds, i.e. during summer time. Besides the lower power of the microbarom source regions during summer time, this can also be a reason for the lower Fisher ratios observed during the summer months.

4.3 1.0 - 6.0 Hz band sources

As seen in Figure 3.14, most higher energetic coherent signals are detected during summer time. The prominent annual concentration of events from the NNE is only observed during July and August, whereas the most other sources are active only later, or at least longer, in summer. Based on observations and information of the local station operator of I18DK, we believe that this NNE source is a turbulent stream of water coming from the local ice cap of Piulup Nunâ.

Just as the number of resolved back-azimuths of the detections in the lower frequency band are plotted as great circle arcs on a sphere, the back-azimuth distribution for the higher frequencies can be plotted in a rose diagram. Besides the distinct energy observed from the NNE, a few specific directions point to sources that are continuously highly active. These horizontal red lines in Figure 3.14 are most distinct during July, August and September. We have superimposed a rose diagram showing the back-azimuth distribution of the detections having Fisher ratios higher than 5 on the map of page 14. This rose diagram (Figure 4.9) is centered on the location of I18DK. We have only used the detections for the months of September, because the events from the NNE are absent for this month. The bin of one degree in width with the highest number of detections, sets the maximum scale value of the bars.

Four distinct peaks pointing south can be observed. Each and every single one of these peaks point straight to a glacier flowing from the ice cap south of the bay into the Inglefield Bredning. That calving glacier ice is capable of producing substantial infrasound signal is showed earlier by *Campus* (2004). The source of the signals from the west-southwest and west-northwest are unknown to us. In any case, the events from a west-southwest direction are probably generated at the tip of the island Herbert Ø, because further on in that direction there's ocean for hundreds of kilometers. So either these detections are due to a source at the tip of Herbert Ø, which could be pack ice being squeezed and pushed up the rocks of this tip or icebergs scraping along the coastline, or there is an ocean based



Figure 4.9: Rose-diagram showing the distribution of the strong events, i.e. Fisher ratio higher than 5, detected for the months September. For every back-azimuth degree, the number of detections is counted. The total number of detections displayed in the rose diagram is 5507 ($\sim 18\%$ of all detections) and the longest bar corresponds to a maximum of 232 detected events from a direction of $192^\circ - 193^\circ$.

source in that direction. The peak to $237^\circ - 238^\circ$ is remarkable, because it's directed along a line that doesn't intersect any mainland or island for hundreds of kilometers. The same statement holds for the peak to the west-northwest. However, both peaks could be due to the scraping of icebergs along the coastline as well, because during August and September the prevailing wind comes from the north as we have derived from the comparison of the apparent velocities of the detections with C_{air} .

In Figure 4.10 the rose diagrams for July (left) and August (right) are shown. During August, the four glaciers produced a significant number of strong infrasound signals as well. July only shows two of the directions corresponding to the glaciers. The bar corresponding to the back-azimuth (1 degree in width) with the highest number of detections sets the maximum scale value of the rose diagram, so the enormous number of strong signals (1118) from the north-northeast in July devaluates the number of detections from the glaciers.

Numerous coherent energetic events are originated to the east-southeast during August.

These detections could well be the microbaroms observed from the same direction in the lower frequency band (see Figure 3.7). To a less extent these signals are detected during the month September as well (see Figure 4.9). Furthermore, during other periods of low local wind speeds like February 2005 and April 2006 the signals from this direction are observed as well (compare Figures 3.3 and 3.14). This would mean that either the high pass slope of the 2nd order 1.0 - 6.0 Hz band pass Butterworth filter isn't sufficient to outweigh the slope of the ocean wave peak, or there are microbaroms generated having a frequency higher than 1.0 Hz. These detections are only visible in Figure 3.14 during periods of low local wind speeds.

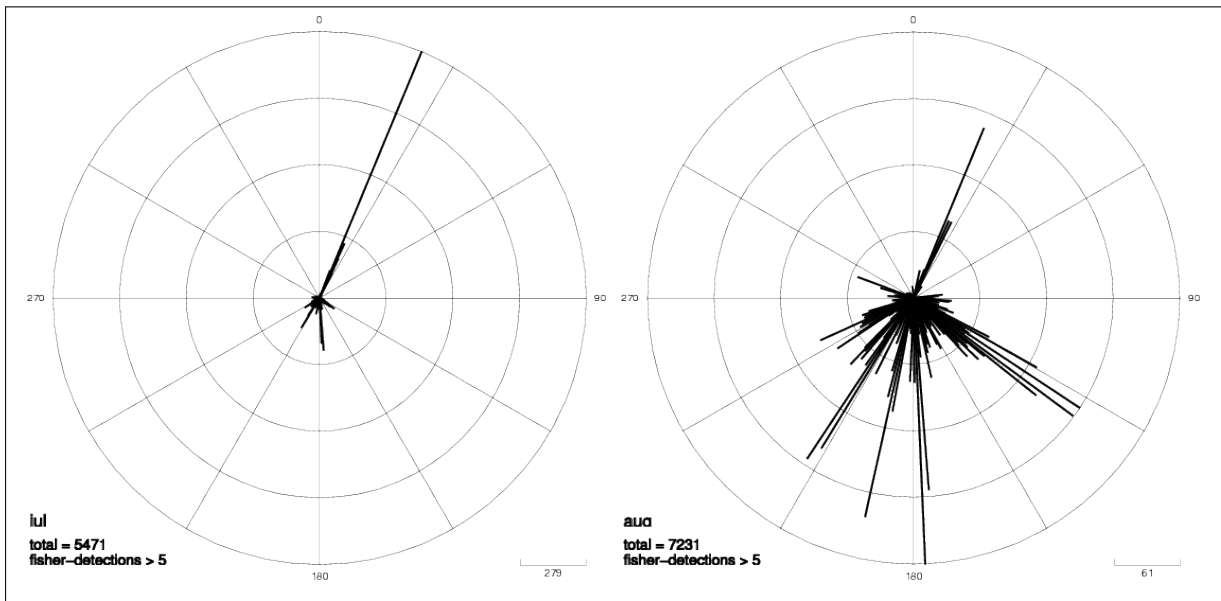


Figure 4.10: Rose-diagrams showing the distribution of the strong events, i.e. Fisher ratio higher than 5, detected in the months July (left) and August (right). For every back-azimuth, the number of detections is counted. The total number of detections displayed in the rose diagrams is 5407 ($\sim 18\%$ of all detections) and 7231 ($\sim 24\%$ of all detections) for July and August respectively. The longest bar corresponds to a maximum of 1118 detected events from a direction of $22^\circ - 23^\circ$ in July and a maximum of 245 events with a back-azimuth of $177^\circ - 178^\circ$ for the months August.

Using the temperature data of I18DK, we have tried to correlate the number of events with a Fisher ratio higher than 5 from the directions of the glaciers with the local temperature. Figure 4.11 shows, for each of three of the southern glaciers, the number of events per day originated to the direction of the glacier. Only events for the four summer months are showed for each year, i.e. approximately from that moment in the year, that the mean day temperature is above zero.

The number of events only starts to increase after the mean day temperature has been above zero for a substantial period. No one-to-one correlation can be found between the daily mean temperature and the number of events detected from the direction of one of the three glaciers. This is not surprising as the dynamics of calving glaciers is extremely

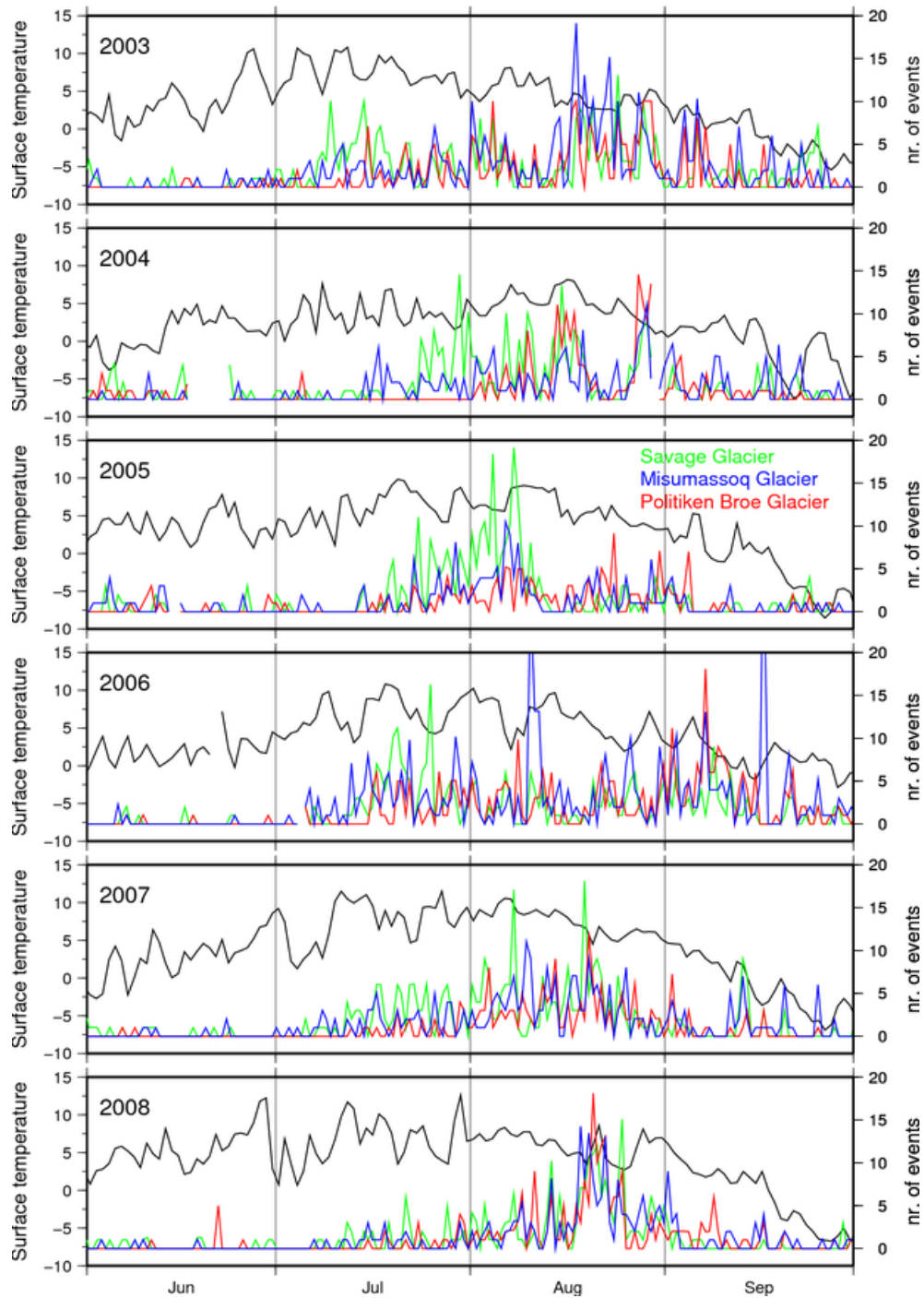


Figure 4.11: Number of events from the direction of the three main glaciers on the South side of Inglefield Bredning compared with the mean day temperature (black line). The following back-azimuths ranges are used to count the number of events corresponding to the concerning glaciers. Savage Gletscher: $175^{\circ} - 181^{\circ}$ (green), Misumassoq Gletscher: $210^{\circ} - 216^{\circ}$ (blue), Politiken Broe: $190^{\circ} - 195^{\circ}$ (red). The black graph shows the variation of the mean day temperature.

complex and depends on a lot of variables. *Benn et al.* (2007) argue that a hierarchy of calving processes can be defined to distinguish between processes that exert a fundamental control on the position of the ice margin and the more local processes that are responsible for individual calving events. According to them, the first-order control on calving is the strain rate arising from spatial variations in flow velocity. The second-order processes determining the calving behavior of a glacier are numerous and not a single one of them has an immediate effect on the calving, i.e. having a time delay of only a few days of the actual increase/decrease of the calving and the process causing it. Even worse, most processes influencing the rate of calving of a glacier only start to effect the actual calving rate after years [*Oerlemans* (2009)].

With the last paragraph in mind, it is not surprising that also Figure 4.12 doesn't show clear correlation between the cumulative temperature and the cumulative number of events from one of the glaciers. The cumulative temperature is the sum of the mean day temperatures. Only mean day temperatures having values above zero are summed as only these days can trigger melting of the ice and possible increased calving of the glacier. The results of Figure 4.12 suggest that temperature is only a second-order process, i.e. there is an increase in calving of the glacier due to higher temperatures, but the total number of calving events in one year is still mainly dependent on the strain rate of the glacier. The summer of 2008, for example, is warm compared to the other summers, but the number of cumulative events detected from the direction of the glaciers doesn't show a significant increase with respect to the other years.

An important note to the above statements must be made. The strength of other sources than the glaciers, is very important concerning the comparison of the cumulative number of events from the directions of the glaciers with the cumulative temperature. If the filtering will be applied more sufficient and the grid search is performed with slowness vectors having a positive north-south component only, i.e. only search for northward traveling coherent energy, the comparison from year to year will be more meaningful. Less counted strong events from the southern glaciers can also be caused by more strong events from the north-northeast source for example.

We believe that this NNE source is a turbulent stream of water coming from the local ice cap of Piulup Nunâ. For this reason we have compared the number of events, i.e. Fisher ratio higher than five, coming from this direction with the number of days with a mean temperature higher than five° C. This comparison is made for each year. Argument for this approach is that the run-off from the local ice cap to the north is related to the degree of melting. As you can see in figure 4.13, there is a high degree of similarity between these two attributes, i.e. a lot of days with a mean temperature higher than five in a year relates to a high number of events from the 20° - 26° back-azimuth range in that same year.

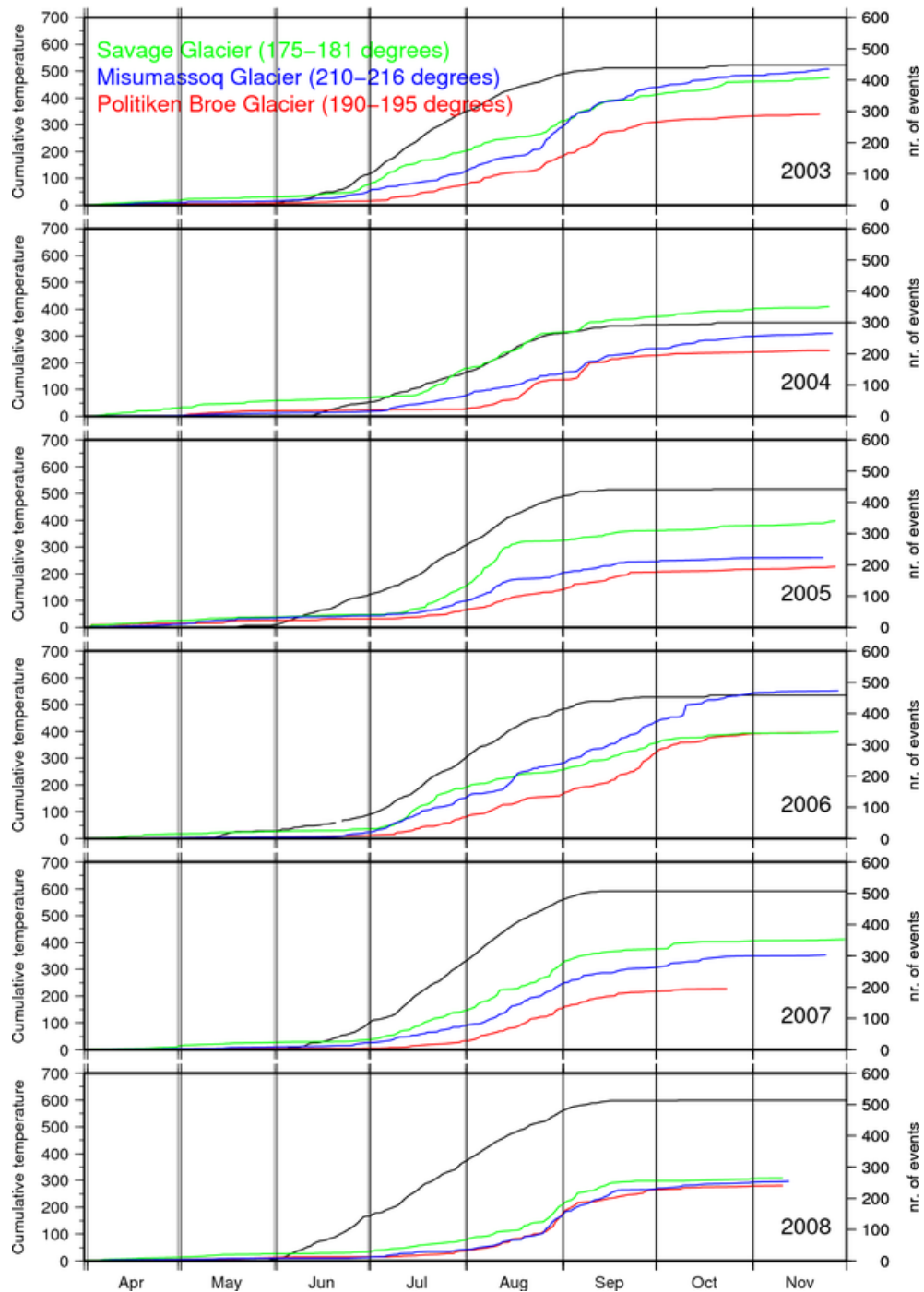


Figure 4.12: Cumulative number of events from the direction of the three main glaciers on the South side of Inglefield Bredning compared with the cumulative day temperature (black line). The following back-azimuths ranges are used to count the number of events corresponding to the concerning glaciers. Savage Gletscher: 175° - 181° (green), Misumassoq Gletscher: 210° - 216° (blue), Politiken Broe: 190° - 195° (red). The black graph shows cumulative mean day temperature.

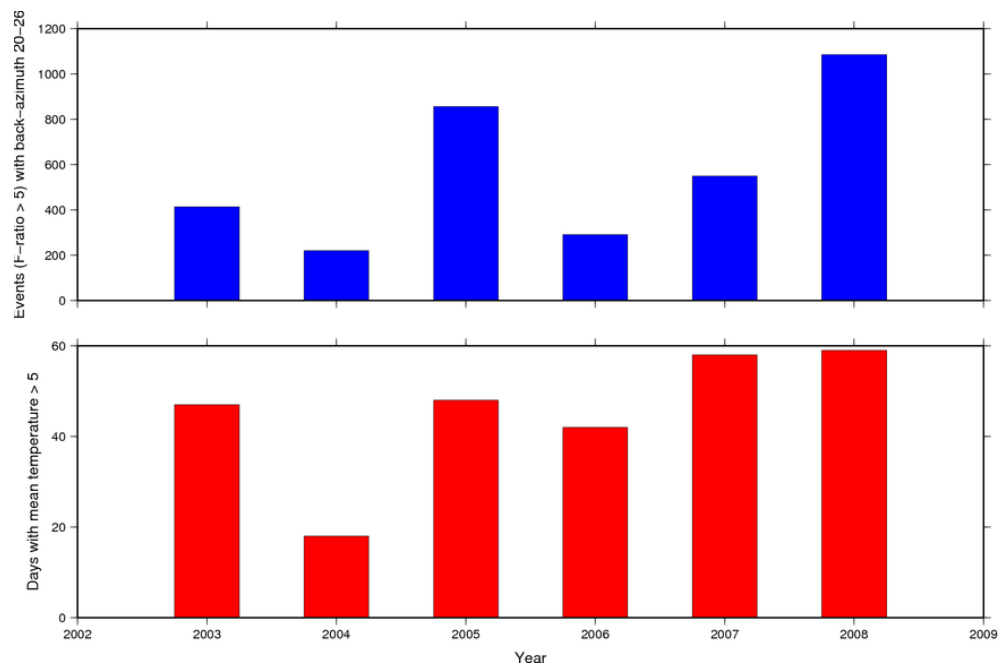


Figure 4.13: The positive correlation between the number of hot days (mean $T > 5^{\circ}\text{C}$) and the total number of events with a F-ratio > 5 from the direction of the Qânâq Gletscher is clear

Chapter 5

Conclusions

Several conclusion can be drawn from this research. A diurnal variation in the hight of the Fisher ratios can be found during summer time. These variations are caused by diurnal variations in the wind speed over the array. Increased wind speeds break down the correlation over the array during daytime yielding lower Fisher ratios. Stabilization of the boundary layer during night time results in higher Fisher ratios.

In the frequency band of 0.1 -1.0 Hz, the strongest signals are coming from the 120° - 150° back-azimuth range and from approximately 280° . These events travel with higher horizontal velocities, i.e. θ has a higher value for these detections. Their origin can be explained by microbaroms over the oceans. A high degree of coincidence between the wave-wave interaction intensity regions produced by *Kedar et al.* (2008) for November 2003 and the directionality of the events measured by I18DK is found.

The dominant back-azimuth of the low frequency detections (0.1 - 1.0 Hz band) is guided by the wind direction at upper stratospheric levels. During spring and fall the reversal of the polar vortex is clearly observed in the dominant back-azimuths of the detections. The microbaroms generated on the Pacific ocean show up in the infrasound analysis results during fall and disappear again at the end of spring time.

Highest Fisher ratios in the 1.0 - 6.0 Hz band are observed during summer time. The events originated to the south of I18DK can be related to the calving of ice from glaciers. At the end of the summer these sources seem to be most active. A turbulent stream of water flowing from the ice cap north-northeast of I18DK seems to be responsible for significant infrasound coming from this direction.

Bibliography

- Arendt, S., and D. C. Fritts (2000), Acoustic radiation by ocean surface waves, *J. Fluid Mech.*, *415*, 1–21.
- Bass, H. E., H. J. Bauer, and L. B. Evans (1972), Atmospheric absorption of sound: Analytical expressions, *J. Acoust. Soc. Am.*, *52*, 821–825.
- Bedard Jr., A. J. (1989), Detection of avalanches using atmospheric infrasound, in *Proc. of Western Snow Conference*, pp. 52–58, Fort Collins, CO, U.S.
- Bedard Jr., A. J. (1994), An evaluation of atmospheric infrasound for monitoring avalanches, in *Proceedings of 7th International Symposium on Acoustic Sensing and Associated Techniques of the Atmosphere and Oceans*, pp. 13–22, NOAA/ERL/Environmental Technology Laboratory, Boulder, CO, U.S.
- Bedard Jr., A. J., G. E. Greene, J. Intrieri, and R. Rodriguez (1988), On the feasibility and value of detecting and characterizing avalanches remotely by monitoring radiated sub-audible atmospheric sound at long distances, in *Proc. Conf. on A Multidisciplinary Approach to Snow Engineering*, pp. 267–275, U.S. Army Corps of Engineers, Cold Regions Research and Engineering Laboratory, Santa Barbara, CA, U.S.
- Benn, D. I., C. R. Warren, and R. H. Mottram (2007), Calving processes and the dynamics of calving glaciers, *Earth-Science Reviews*, *82*, 143–179.
- Bowman, J. R. (2005), Meteorological conditions at infrasound stations, *Inframatics: The newsletter of subaudible sound*, *9*, 17–26.
- Bowman, J. R., G. E. Baker, and M. Bahavar (2005), Ambient infrasound noise, *Geophys. Res. Lett.*, *32*(L09803), doi 10.1029/2005GL022486.
- Campus, P. (2004), The IMS infrasound network and its potential for detection of events: Examples of a variety of signals recorded around the world, *Inframatics: The newsletter of subaudible sound*, *6*, 13–22.
- Capon, J. (1969), High-resolution frequency-wavenumber spectrum analysis, *Proceedings of the IEEE*, *57*, 1408–1418.

- Cohen, L., W. D. Neff, A. A. Grachev, and C. W. Fairall (2007), Boundary-layer dynamics and its influence on atmospheric chemistry at Summit, Greenland, *Atmospheric Environment*, *41*(24), 5044–5060.
- Cullen, N. J., and K. Steffen (2001), Unstable near-surface boundary conditions in summer on top of the Greenland ice sheet, *Geophys. Res. Lett.*, *28*(23), 4491–4493.
- Donn, W. L., and B. Naini (1973), Sea wave origin of microbaroms and microseisms, *J. Geophys. Res.*, *78*, 4482–4488.
- Drob, D. P., and J. M. Picone (2003), Global morphology of infrasound propagation, *J. Geophys. Res.*, *108*(D21), 4680–4693.
- Ekström, G., M. Nettles, and V. C. Tsai (2006), Seasonality and increasing frequency of Greenland glacial earthquakes, *Science*, *311*(5768), 1756–1758.
- Evers, L. G. (2008), The inaudible symphony: On the detection and source identification of atmospheric infrasound, Ph.D. thesis, Delft University of Technology, Delft, The Netherlands.
- Evers, L. G., and J. Schweitzer (2010), A climatology of infrasound observations at the ARCI array in Norway, in preparation.
- Fisher, R. A. (1948), *Statistical Methods for Research Workers*, Oliver and Boyd, London, UK.
- Google Inc. (2009), Google maps, <http://www.googlemaps.com>.
- Gossard, E. E., and W. H. Hooke (1975), *Waves in the Atmosphere*, Elsevier Scientific Publishing Company, Amsterdam, The Netherlands.
- Kaimal, J. C., and J. J. Finnigan (1994), *Atmospheric Boundary Layer Flows: Their Structure and Measurement*, p. 289, Oxford University Press, Inc., Oxford.
- Kedar, S., M. Longuet-Higgins, F. Webb, N. Graham, R. Clayton, and C. Jones (2008), The origin of deep ocean microseisms in the North Atlantic Ocean, *Proc. R. Soc. A*, *464*(2091), 777–793.
- Marchetti, E., M. Ripepe, A. J. L. Harris, and D. D. Donne (2009), Tracing the differences between vulcanian and strombolian explosions using infrasonic and thermal radiation energy, *Earth and Planetary Science letters*, *279*, 273–281.
- Melton, B. S., and L. F. Bailey (1957), Multiple signal correlators, *Geophysics*, *XXII*(3), 565–588.
- NOAA, NASA, and USAF (1976), *US Standard Atmosphere*, U.S. Government Printing Office, Washington D.C., Washington, USA.

- Oerlemans, J. (2009), Personal Communication, (IMAU).
- Posmentier, E. (1967), A theory of microbaroms, *Geophys. J. R. astr. Soc.*, *13*, 487–501.
- Priestley, J. T. (1966), Correlation studies of pressure fluctuations on the ground beneath a turbulent boundary layer, *Tech. Rep. 8942*, U.S. Dept. of Commerce, National Bureau of Standards, Washington D.C.
- Rind, D. (1980), Microseisms at Palisades 3. microseisms and microbaroms, *J. Geophys. Res.*, *78*, 4854–4862.
- Sherrif, R. E., and L. P. Geldart (1995), *Exploration Seismology*, p. 247, 2 ed., Cambridge University Press.
- Shumway, R. H. (1971), On detecting a signal in N stationarily correlated noise series, *Technometrics*, *13*, 499–519.
- Smart, E., and E. A. Flinn (1971), Fast frequency-wavenumber analysis and Fisher signal detection in real-time infrasonic array data processing, *Geophys. J. R. astr. Soc.*, *26*, 279–284.
- Symons, G. J. (1888), *The Eruption of the Krakatoa and Subsequent Phenomena*, Trübner & Co, London, UK.
- Wilson, C. R. (1967), Infrasonic pressure waves from aurora: A shock wave model, *Nature*, *216*, 131–133.
- Woodward, R., H. Israelsson, I. Bondar, K. McLaughlin, J. R. Bowman, and H. Bass (1994), Understanding wind-generated infrasound noise, in *Proceedings of 27th Seismic Research Review: Ground-Based Nuclear Explosion Monitoring Technologies*, pp. 866–875, National Nuclear Security Administration, Rancho Mirage, CA, U.S.